NTNU
Norwegian University of
Science and Technology

Natural Dyes as Candidate Materials for Organic Solar Cells

An Optical, Electronic and Structural Characterisation

Annika Richter

Innovative Sustainable Energy Engineering
Submission date: July 2018
Supervisor: Justin Wells, IFY
Co-supervisor: Jens Wenzel Andreasen, DTU

Norwegian University of Science and Technology
Department of Physics

Preface

This thesis is submitted in partial fulfilment of a dual international MSc in Innovative Sustainable Energy Engineering in the study track Solar Cell Systems and Materials. It was carried out in the spring semester of 2018 in the physics department of NTNU. The body of work corresponds to 30 ECTS. It was supervised by Assoc. Prof. Justin Wells from NTNU. The co-supervisor from the N5T partner university was Prof. Jens Wenzel Andreasen at DTU.

Annika Richter
Trondheim, July 2018

Acknowledgements

First of all, I would like to thank my NTNU supervisor Assoc. Prof. Justin Wells for his far-reaching interpretation of that role. Thank you for taking me to Brazil for this project, for always taking the time to discuss questions (despite having a very short mean free path, as some people say), as well as all the chats and discussions unrelated to photoemission. Secondly I want to thank Prof. Jens Wenzel Andreasen for agreeing to be my DTU supervisor and for his kind support on all issues regarding the technicalities with the DTU system.

It is mainly thanks to Dr. Leander Michels that I got involved in this project, which I am very grateful for. Thank you for all the advice on XRD data analysis, peak fitting and the great tour guiding in Brazil. You rock and no nightshift on a beamline is boring when you are around.
For the countless hours of work put into helping me out in the lab regardless of the time of day, I owe a special thank you to both Dr. Alex Schenk and Dr. Rajesh Kumar Chellappan. Without you, this simply would have been impossible.
A special thank you also goes to our collaborators in Brazil, most importantly Prof. Stefan Michael Blawid, Dr. Luciano Leal and Vilany Santana for the warm welcome in Brasília and the great working atmosphere at LNLS. Additionally I want to thank Vilany for the kind permission to include some of her UV-Vis measurements in this thesis. For his support at the beamline I would like to thank Dr. Antonio Gasperini.
I want to thank Prof. Ursula Gibson and Dr. Mustafa Balcı for the kind permission to use the UV-Vis instrument and for the assistance with the measurements.
Dr. Kristin Høydalsvik Wells I would like to thank for the help with the XRD data analysis in *Topas*.
A very special thank you goes to Frode Sneve Strand for the careful proofreading, many useful discussions and for forcing me out of the lab to take breaks. And for introducing me to the joys of motorbiking of course.

I would also like to seize this opportunity to thank people without which I wouldn't be where I am today. To the MSISEE Solar Crew, Carolyn, Johanna, Kevin and Ruby, we've been a great team through the last 2 years. Keep on making the world a sunnier place!
To my wonderful friends who inspire me across oceans, I can't wait to see what grown-up life holds for us.
To Pablo, thank you for choosing to be a constant in my life. You remain the best teacher I've ever had.
Finally I want to thank my family – My brothers and role models Martin and Stefan, as well as Minna and Annick, who make up for my non-existing sisters. My parents, who have always supported (and funded) all of my endeavours – I've been beyond privileged to be your daughter. And little Ben, who without knowing it has contributed to this work by putting a big smile on my face even in the most stressful of times.

Abstract

Natural dyes strongly absorbing light in the visible spectrum are appealing materials for the use in organic solar cells, due to their direct availability from nature. An especially interesting potential application arises from a reported reduction in charge carrier trapping in organic semiconductors blended with large-band gap compounds. On this account, an optical, electronic and structural characterisation of the natural yellow and red dyes curcumin and bixin was performed, to create a basis for future investigations of their applicability in organic solar cells.

Optical absorption spectra measured by UV-Visible Spectroscopy (UV-Vis) on thermally evaporated films revealed that bixin undergoes chemical degradation upon evaporation, while curcumin appears to remain unaffected. Cheap availability of high purity curcumin and easy processability allowed for reliable determination of its band gap, both from the absorption spectrum, as well as combined Ultraviolet Photoemission Spectroscopy (UPS) and Inverse Photoemission Spectroscopy (IPES). The obtained values of 2.3 eV and 2.4 eV, respectively, are in good agreement with each other. The band gap of bixin was found to be larger than expected (2.5 eV and 2.8 eV, respectively), most likely as a result of the degradation of the molecule and an insufficient film thickness for photoemission measurements free of contributions from substrate contaminants. UPS and IPES spectra furthermore revealed that both curcumin and bixin are hole-conducting materials.

X-ray diffraction (XRD) measurements on powder performed at the Brazilian Synchrotron Light Laboratory (LNLS) in Campinas, Brazil, revealed a higher crystalline order in curcumin than bixin. A Pawley unit cell refinement using the obtained diffraction pattern on curcumin yields the refined lattice parameters $a = 12.7419(3)$ Å, $b = 7.2202(3)$ Å, $c = 20.0530(9)$ Å and $\beta = 94.9801(1)°$, which are in good agreement with those found in literature. After annealing the curcumin powder at 200°C, the signal intensity is found to be decreased, which could be interpreted as an increase in crystalline order with the majority of crystallites oriented such that their reflections cannot be detected with the used geometry of the setup. A diffraction pattern on bixin powder was successfully measured. In future work this could, in combination with computational density functional theory (DFT) calculations, reveal the crystal structure of bixin for the first time. Evaporated as well as solution-cast samples of both dyes proved to be too thin to produce a useful signal in the XRD measurement.

The results show that curcumin has several advantages over bixin in terms of processability, stability and crystalline order, which are favourable properties for organic solar cell applications. Curcumin can therefore be considered a promising candidate material. A meaningful analysis of bixin allowing for a clear conclusion is complicated by difficulties forming sufficiently thick films, as a result of the lack of cheaply available high purity bixin. The observed decomposition of the molecule upon evaporation does not rule it out as a candidate material, but adds to the need for studying solution-processed films made from a cheaper (potentially less pure) form of it.

Contents

1 Introduction

Conventional silicon solar cells have been facing increased competition from quickly developing new generations of solar cell technologies. Especially organic solar cells have attracted a steadily growing academic interest due to their lightness, mechanical flexibility, and inexpensive processing. The first experiments marking the beginning of organic photovoltaics (OPV) sandwiched organic dyes between metal electrodes with a large work function offset [1–3], inspired by the photosynthesis of plants transforming sunlight into chemical energy. Ever since, the search for organic semiconductors suitable for efficient photovoltaic energy conversion has been going on. With cells based on synthesised polymers currently marking the standard in OPV, there is still a lot of work to be done in uncovering the potential of natural materials. In this thesis, natural dyes are investigated to create a basis on which to evaluate their applicability in OPV. The main factors of interest to this effect are the size of the band gap, crystalline order, as well as processability, and stability under heat.
The molecules investigated are curcumin ($C_{21}H_{20}O_6$) and bixin ($C_{25}H_{30}O_4$), shown in Fig. 1. Curcumin is a pigment of turmeric and has been used as a home-remedy against different ailments in India for centuries. It has attracted high scientific attention since the 1990s, mainly due to its reported chemopreventive effect [4, 5]. Bixin is the main carotenoid found in the seeds of the annatto tree, that is native to South America. Given its strong red colour it is commonly used as a dye in textiles, cosmetics and food among other things [6, 7]. As both dyes absorb strongly in the visible spectrum, efforts to use them in dye-sensitised solar cells (DSSC) have already been made [8–10].

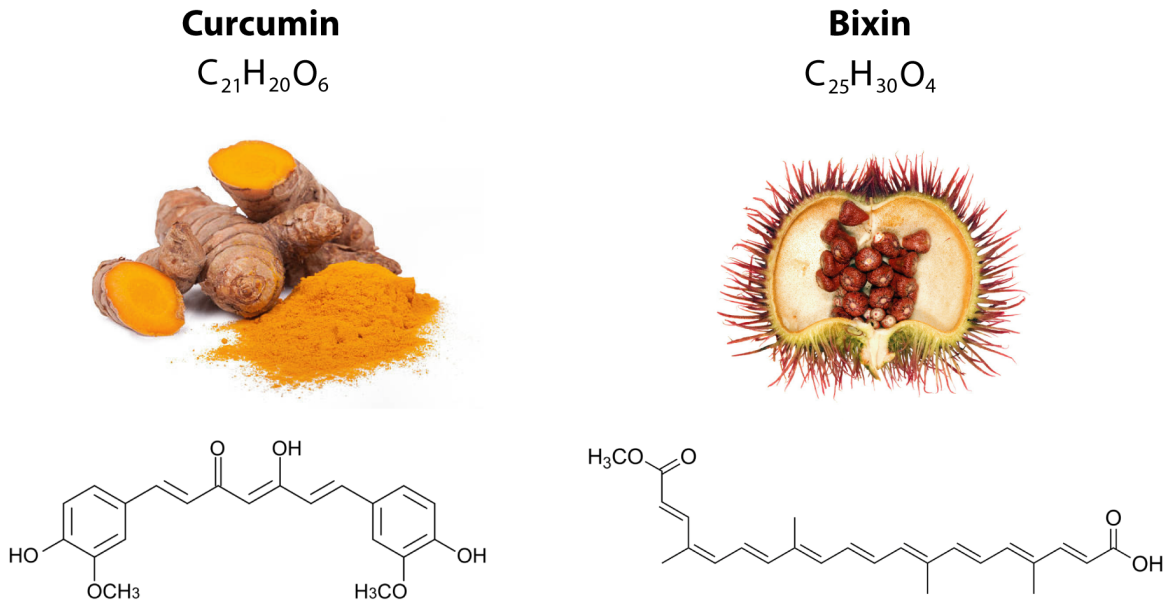

Figure 1: The two molecules investigated in this thesis are the organic dyes curcumin and bixin.

Whether they could be candidates for active layer materials in solid-state organic solar cells to this day remains unstudied. An especially interesting application of large band gap semiconductors like curcumin and bixin could be in blends with conjugated polymers. Such diluted semiconductors have been reported by Abbaszadeh et al. [11] to have

a significantly reduced amount of trapping sites, which leads to increased charge carrier lifetimes.
Using natural materials in organic photovoltaics, as opposed to synthetic polymers is appealing considering that the processing of the latter often requires hazardous halogenated solvents [12]. On top of that, the direct harvesting of useful materials from nature could prove cost-effective.

In the present work, films of curcumin and bixin are prepared by thermal evaporation in vacuum and by solution processing. These films are subjected to a thorough electronic characterisation using different photoemission spectroscopy (PES) techniques. For structural analysis of the films, X-ray diffraction experiments are carried out at the Brazilian Synchrotron Light Laboratory (LNLS) in Campinas, Brazil. Additionally, UV-Visible Spectroscopy (UV-Vis) is performed to check the optical absorption characteristics of the thermally evaporated films. Most measurements are to the author's best knowledge the first of their kind to be performed on bixin, as up to this day very little literature has been published about this compound.

In Chapter 2, underlying theoretical concepts relevant to this work will be presented. These include basics on organic semiconductors and photovoltaic devices, and the theory behind photoemission spectroscopy and X-ray diffraction, which are the main experimental techniques used in the work. Chapter 3 will present details on the different methods of sample preparation, the vacuum system used for the photoemission experiments and the setup of the individual experiments. It also presents the photospectrometry setup used for measuring absorption spectra and the experimental setup at the beamline at LNLS. In Chapter 4, main results of all experiments are presented and discussed. Chapter 5 gives a conclusion of the most important results as well as an outlook to future investigations.

2 Theory

In this section the key concepts underlying the presented work will be introduced. The first part gives a short overview of organic solar cell materials and working principles. It is followed by a presentation of the theory behind the main experimental techniques used in this work – photoemission spectroscopy and X-ray diffraction.

2.1 Organic Solar Cells[1]

2.1.1 Organic semiconductors

An organic semiconductor is a carbon-based material with semiconductor properties, i.e. a band gap. This band gap arises from a structure of alternating single and double bonds of sp^2-hybridised carbon atoms, forming a so-called conjugated system. The sp^2 hybridised orbitals form strong σ bonds between neighbouring carbon atoms. As only three of the four valence electrons of the carbon atoms hybridise in the sp^2 configuration, the remaining unhybridised p orbitals form delocalised π bonds. In the energetically favoured, and therefore stable state, the density of the π electrons is concentrated between neighbouring carbon atoms in the bonding (π) configuration, leaving the antibonding (π^*) orbital unoccupied (see Fig. 2). The π orbital is therefore the Highest Occupied Molecular Orbital (HOMO), while the π^* orbital in this configuration is the Lowest Unoccupied Molecular Orbital (LUMO).

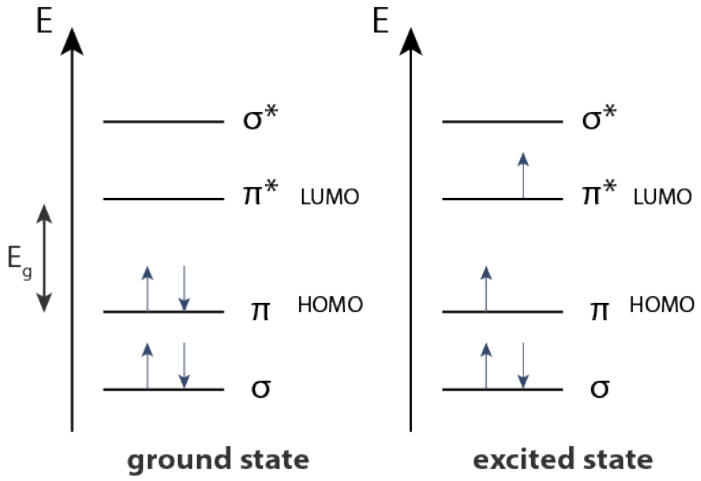

Figure 2: Molecular orbital diagram of an alkene. The left side shows the electron configuration in the ground state. When energy is absorbed, electrons can be transferred from the π orbital to the π^* orbital, leaving the molecule in an excited state, shown on the right side. Based on reference [18].

The HOMO and the LUMO correspond to the valence band and the conduction band in an inorganic semiconductor and can be treated similarly on a macroscopic level. The energy difference between the HOMO and the LUMO is the band gap E_g. When the molecule is excited by a sufficiently energetic photon, electrons can be transferred from the bonding π band to the antibonding π^* band. As opposed to an inorganic semiconductor, where this transition is an actual excitation of a free electron from the valence band to the conduction band, here the molecule itself is excited to a more energetic state.

[1] This section is based on references [13–17].

2.1.2 Working principle of an organic solar cell

An organic solar cell (OSC) is a solar cell made of organic semiconductors. As described above, the absorption of a photon in an organic semiconductor can excite electrons from the HOMO to the LUMO. The resulting electron-hole pair in organic photovoltaics is called an exciton. This term acknowledges the strong Coulombic attraction between the electron-hole pairs in organic semiconductors as opposed to those in inorganic semiconductors. The binding energy of such a pair is around 0.1–1.4 eV [19].
The separation of electron-hole pairs to generate electricity in an OSC occurs in the so-called active layer, which is formed by a heterojunction of two materials with a suitable band alignment. Fig. 3 illustrates the working principle of the active layer. First, an exciton is generated in one of the materials (Fig. 3.1). When the difference between the HOMO of the first material and the LUMO of the second material is smaller than the potential difference between the bound electron–hole pair, an exciton that is generated in the first material moves towards the junction (Fig. 3.2), where it is energetically favourable for the electron of the exciton to transfer to the LUMO of the second material (Fig. 3.3). Because of this charge transfer the two materials are referred to as donor and acceptor. Finally, the holes are transported to an anode electrode and the electrons to a cathode electrode through a potential gradient established by the choice of electrode or transport layer materials (Fig. 3.4). This gradient can for example be established by choosing a high work function material for the anode and a low work function material for the cathode.

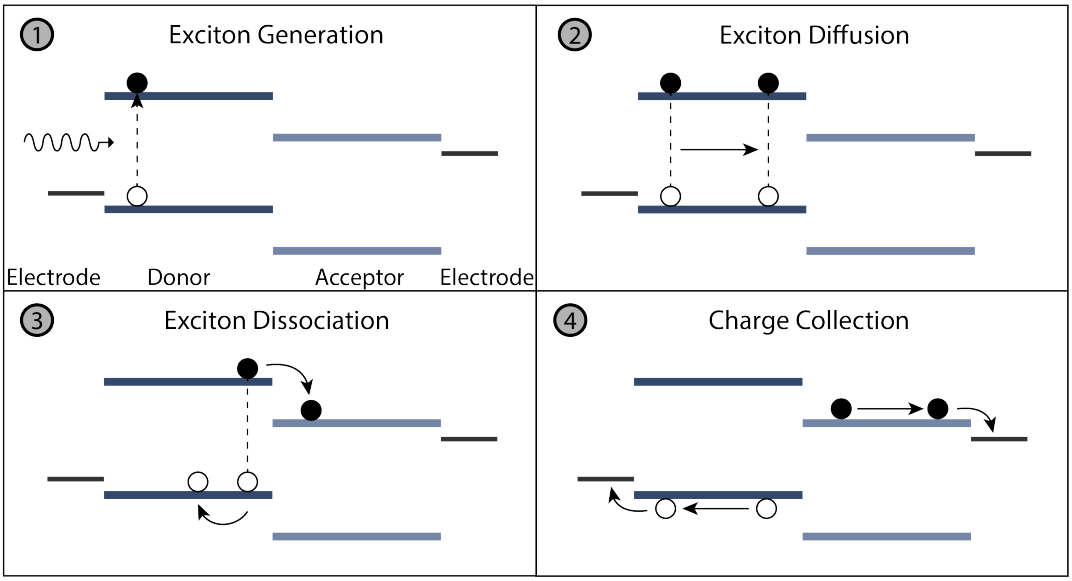

Figure 3: Principle of charge separation in an organic solar cell. (1) An exciton is generated by photon absorption. (2) The exciton diffuses to the donor/acceptor heterojunction. (3) The exciton dissociates at the junction. (4) The carriers are transported and extracted at the electrodes. Based on reference [13].

A typical structure of an organic solar cell is shown in Fig. 4. The individual layers are normally stacked on top of each other onto a substrate by printing and coating methods. The charge generation and separation happens in the active layer, which is surrounded by two transport layers allowing only a certain carrier type to pass, and finally the electrodes to extract the current from the solar cell.

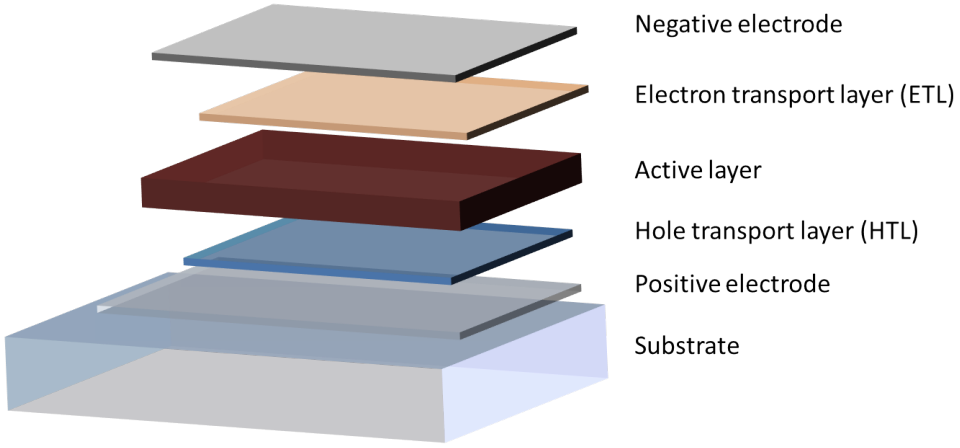

Figure 4: Structure of an organic solar cell. Adapted from reference [18].

2.1.3 Active layer materials

The active layer forms the key part of the organic solar cell, as this is where the charge generation and separation occurs. Therefore a large part of the research in organic photovoltaics is focused on the materials used in the active layer. The most important characteristic of an organic semiconductor for the use in solar cells is its band gap, defined as the energy gap between the HOMO and the LUMO:

$$E_g = E_{\mathrm{LUMO}} - E_{\mathrm{HOMO}}. \tag{1}$$

For a photon to be absorbed by the semiconductor its energy must be greater than or equal to E_g:

$$E_{\mathrm{photon}} = h\nu = \frac{hc}{\lambda} \geq E_g, \tag{2}$$

where h is Planck's constant, ν is the frequency of the photon, c is the speed of light and λ is the wavelength of photon. When the photon energy exceeds the band gap, the excess energy is lost as heat. From Eq. 2, one can establish the optimal size of the band gap for a single junction solar cell, given the spectrum of solar irradiance inside the atmosphere. This was first done by Shockley and Queisser, who in 1960 published a paper [20], in which they introduced the now famous curve seen in Fig. 5 (black line). It shows the maximum theoretical power conversion efficiency of a single junction solar cell as a function of its band gap (assuming AM 1.5 solar spectrum and unconcentrated sunlight). The maximum value of around 33.7% occurs at a band gap of 1.34 eV.

The active layer materials used in organic photovoltaics are small molecules or polymers with conjugated π-bonds, as discussed in section 2.1.1. Their band gap is typically in the range of 1 to 3eV [22] and depends, among other things, on the conjugation length (i.e. the length of undisturbed conjugations); a shorter conjugation length resulting in a larger band gap [23]. This allows for tuning the band gap to a desired size by synthetic modification.
The current record efficiency reported for an organic solar cell of 11.2% [24] is still far from reaching the theoretical limit of maximum efficiency. A major challenge in the design of organic solar cells is the very short diffusion length of excitons of around 5–20 nm [25–27],

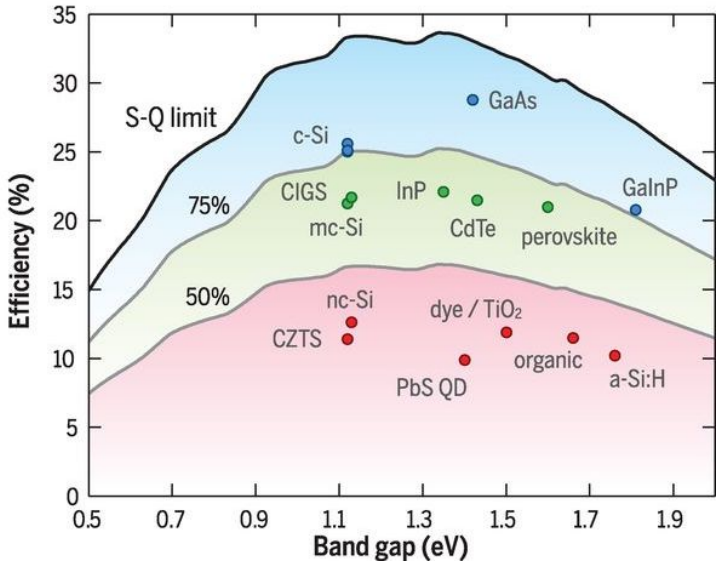

Figure 5: Theoretical Shockley-Queisser power conversion efficiency limit as a function of band gap (black line) and 75% and 50% of the limit (grey lines). The markers show record efficiencies reported for different materials (from 2016). Adapted from reference [21].

before they recombine. This places constraints on the morphology of the active layer and creates a need to minimise recombination sources.

2.1.4 Optical absorption

When studying solar cell materials, optical absorption properties play a central role. A characteristic of all semiconductors is the sudden increase in absorption (a so-called absorption edge) when the condition in Eq. 2 is met. For photon energies below the band gap, the semiconductor is transparent.
Absorption attenuates the intensity of a light beam as it propagates through the material. This is mathematically described by the Beer-Lambert law. It states that the intensity of light I at a depth x in the materials is given by

$$I(\lambda, x) = I_0(\lambda)e^{-\alpha(\lambda)x}, \tag{3}$$

where I_0 is the incident intensity at $x = 0$ and α is the optical absorption coefficient, which is an important parameter for describing solar cell materials. Organic semiconductors have been found to possess very high absorption coefficients ($> 10^5\,\mathrm{cm}^{-1}$), which is a key prerequisite for thin active layers [13].
The transmittance of the material is then described by

$$T = \frac{I}{I_0}. \tag{4}$$

This is a quantity that can easily be determined experimentally by passing a beam through a sample and measuring the intensity before and after. Another commonly used quantity is the absorbance A, which is related to the transmittance via

$$A = -\ln(T) = \alpha(\lambda)x. \tag{5}$$

As the absorbance is directly proportional to the path length, it can be used to determine the absorption coefficient of the material, when the sample thickness is known.

2.2 Photoelectron Spectroscopy (PES)[2]

2.2.1 Basic principles

Photoelectron Spectroscopy (PES), also called Photoemission Spectroscopy, is an experimental method to study the electronic structure and chemical state of atoms and molecules. It is based on analysing the energy of electrons emitted from a solid after excitation with energetic photons. The process is commonly described using the so-called *three-step model*, in which it is separated into three individual processes, which are illustrated in Fig. 6. In the first step, an electron is excited in the solid by absorbing a photon. In the second step, the photoelectron travels through the solid towards the surface. In the third and final step, the electron is then emitted into the vacuum where it is detected.

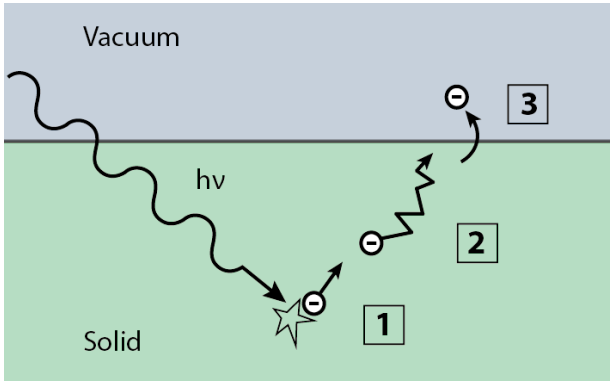

Figure 6: Schematic representation of photoemission as a three-step process: (1) photoexcitation of an electron, (2) transport of the electron to the surface, (3) penetration through the surface. Based on reference [29].

The resulting photoemission intensity or photoemission current measured by the detector, which is a function of the kinetic energy of the photoelectron in vacuum E_{kin} and the photon energy $h\nu$, is then proportional to the product of the probabilities associated with each individual step. If these probabilities are described by $\mathrm{P}(E_{\mathrm{kin}},h\nu)$, $\mathrm{T}(E_{\mathrm{kin}},h\nu)$ and $\mathrm{D}(E_{\mathrm{kin}})$ respectively, for the photoemission intensity I we have

$$I \sim \mathrm{P}(E_{\mathrm{kin}}, h\nu)\mathrm{T}(E_{\mathrm{kin}}, h\nu)\mathrm{D}(E_{\mathrm{kin}}). \tag{6}$$

For electron energies $E_{\mathrm{kin}} > 100\,\mathrm{eV}$ it can be assumed that the probabilities of step two and three are independent of E_{kin}, in which case the resulting photoemission spectrum directly reflects $\mathrm{P}(E_{\mathrm{kin}},h\nu)$. This is the parameter that contains the information on the electronic states of the solid in the initial state. $\mathrm{T}(E_{\mathrm{kin}},h\nu)$, representing the probability that a photoelectron is transported to the surface without being seriously affected by inelastic scattering, is dependent on the absorption coefficient for the incident photon energy and the electron inelastic mean free path (IMFP) that is discussed in section 2.2.4. $\mathrm{D}(E_{\mathrm{kin}})$ depends gently on E_{kin} and on the work function of the material.

A schematic of a typical PES setup is shown in Fig. 7a. The main parts of the system are the photon source and the electron energy analyser that determines the kinetic energy of the ejected photoelectrons. Due to the very small mean free path of the photoelectrons, the system needs to be situated in an ultra-high vacuum (UHV) environment (c.f. section

[2]This section is based on references [28, 29].

2.2.4).

From the measured kinetic energy E_{kin} of the electrons, their binding energy E_{B} can then be determined according to

$$E_{\mathrm{B}} = h\nu - E_{\mathrm{kin}} - \phi_{\mathrm{S}}, \tag{7}$$

where $h\nu$ is the energy of the incoming photons and ϕ_S is the work function of the sample. This is valid in a solid where E_{B} is typically defined with respect to the Fermi level E_{F}. The binding energy spectrum is characteristic of the analysed material, which is the reason why PES can be used for determining elemental composition.

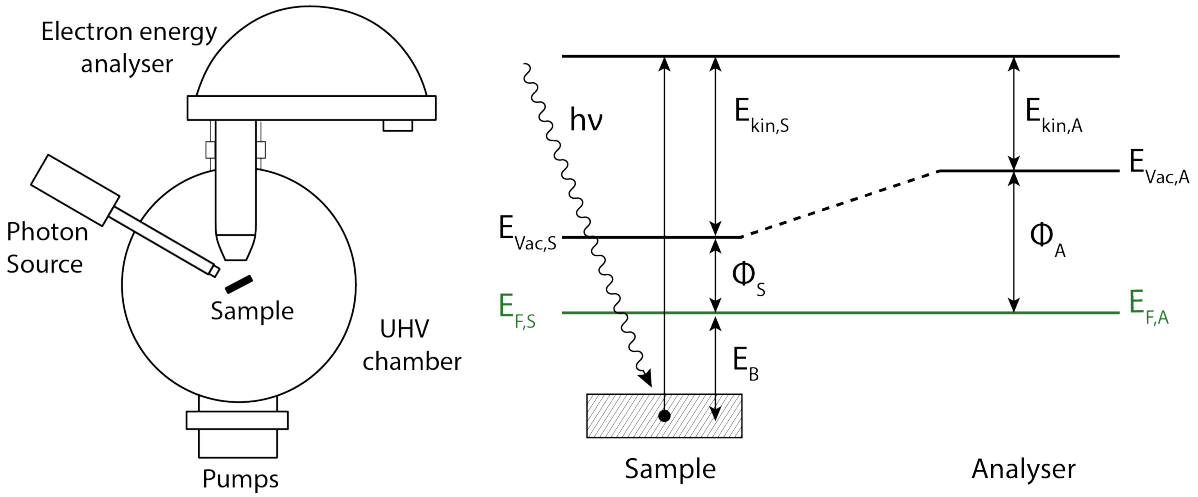

(a) (b)

Figure 7: **(a)** Schematic of a photoemission spectroscopy system setup **(b)** Photoelectrons leave the sample with a kinetic energy of $E_{\mathrm{kin,S}}$, but are recorded in the spectrometer with an energy $E_{\mathrm{kin,A}}$ due to the difference in work functions of the sample and the analyser.

The analyser possesses a work function ϕ_{A}, that is different from the work function of the sample ϕ_{S}. When a conductive connection between the analyser and the sample is established, their Fermi levels align. As a result of this, the kinetic energy measured by the spectrometer $E_{\mathrm{kin,A}}$ differs from the kinetic energy of the free photoelectrons $E_{\mathrm{kin,S}}$ by the difference in work functions ($\phi_{\mathrm{A}} - \phi_{\mathrm{S}}$). This is illustrated in Fig. 7b. Consequently, the binding energy can be determined without the need to know the work function of the sample, after a one-time calibration of the analyser work function:

$$E_{\mathrm{B}} = h\nu - E_{\mathrm{kin,A}} - \phi_{\mathrm{A}}. \tag{8}$$

In Fig. 8 the relation between the energy levels in a solid (in this case a metal) and the energy distribution of photoemitted electrons is illustrated schematically.
Different photon energies are used to probe different parts of the spectrum. PES is generally divided into Ultraviolet Photoelectron Spectroscopy (UPS) operating in the ultraviolet regime from 5 to 100 eV and X-ray Photoelectron Spectroscopy (XPS) operating in the X-ray regime of >100 eV. The most commonly used photon energies in UPS are the HeI line (21.2 eV) and the HeII line (40.8 eV) emitted from gas discharge lamps. In XPS, sources traditionally include X-ray tubes using the magnesium K_α line (1263.6 eV) and

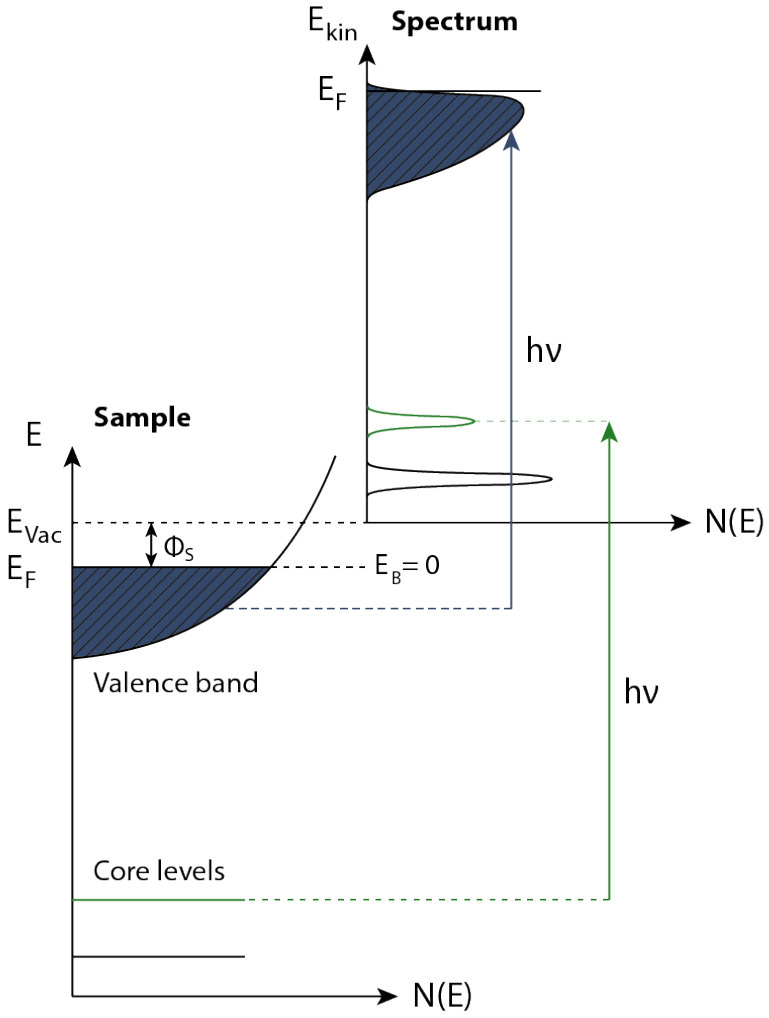

Figure 8: Schematic energy diagram illustrating the relation between energy levels in the sample and the measured photoemission spectrum. Based on references [28] and [30].

the aluminium K_α line (1486.6 eV), as well as synchrotron radiation sources, ever since they have become available. XPS allows for the investigation of core levels, which can be used for chemical analysis of the samples. For studying the valence band, UPS however provides higher accuracy.

2.2.2 Features of an XPS spectrum

In reality, an XPS spectrum does not look like the spectrum presented in Fig. 8. In addition to photoemission peaks, a broad background signal is created from electrons that are inelastically scattered before reaching the analyser. Furthermore, a number of effects create additional features in the spectrum, that shall be introduced in the following.

Auger peaks

At high photon energies the spectrum will exhibit peaks resulting from Auger electrons. These are produced when a vacancy created by an incoming photon is filled by the decay of an electron from a higher shell and an electron with an energy equal to the difference between the involved states is emitted. Consequently, the kinetic energy of the Auger

electrons is independent of the photon energy of the source. Fig. 9 illustrates the process of Auger electron emission compared to photoelectron emission.

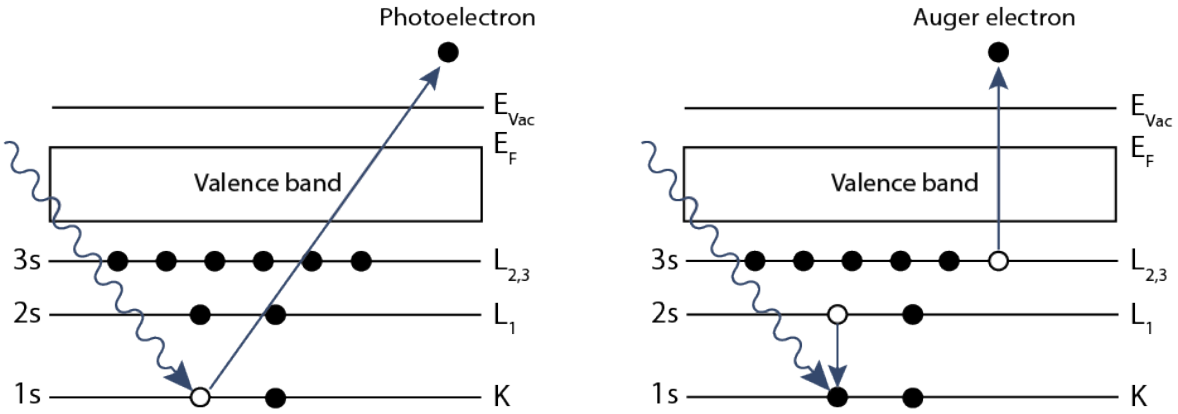

Figure 9: Schematic diagram illustrating the emission process of a photoelectron from a core level into vacuum (left) and that of an Auger electron (right).

Chemical shifts

Core level photoelectron spectra do not only provide information on the elements present in the sample but also on the local environment of the atoms, i.e. the configuration of chemical bonds. These give rise to shifts in binding energy, that are referred to as chemical shifts.
The observed chemical shift in a spectrum is generally attributed to two factors. The first contribution is the initial state effect that essentially consists of changes in electrostatic screening of core orbitals, as caused by ionic bonding. This effect is illustrated in Fig. 10 on the Li1s level in lithium metal and lithium oxide. In pure lithium metal, the binding energy is lower due to increased screening of the nucleus by 2s conduction electrons (Fig. 10a). In lithium oxide (Li_2O), the oxygen atom withdraws electron density from the 2s orbital of the lithium atoms, whereby the binding energy increases (Fig. 10b). The resulting photoelectron spectrum of the Li1s level shows two separate peaks for lithium metal and lithium oxide, shifted by a characteristic distance (Fig. 10c).

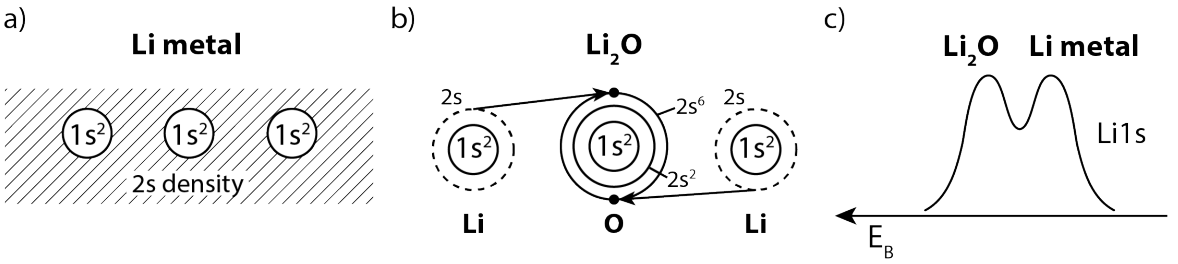

Figure 10: Schematic illustration of **a)** the electron configuration in Li metal, **b)** in Li_2O and **c)** the corresponding Li1s PES spectrum (schematically drawn). The Li_2O core electron is more tightly bound due to electron density withdrawal from the Li atoms by the O atom in the outer valence shells. Based on reference [28].

The second contribution to the chemical shift arises from differences in the relaxation energy, when the hole left by a liberated core electron is filled by a more energetic electron. This final state contribution however is generally much smaller than the initial state one and therefore often neglected.

Spin-orbit splitting

Another feature observed in XPS spectra results from shifts in the atomic energy levels due to spin-orbit coupling. This is the interaction between the orbital angular momentum l of electrons and the spin magnetic dipole $s = \frac{1}{2}$, which leads to the splitting of energy states that would otherwise be degenerate. For each shell, the total angular momentum that is given by $j = |l \pm s|$ can take two different values (except s orbitals, for which $l = 0$). This splitting of states is reflected in the XPS spectrum in two separate peaks, which are referred to as doublet pairs. The ratio of intensities of doublet peaks is given by

$$r = \frac{2(l+s)+1}{2(l-s)+1}. \tag{9}$$

So p orbital doublets with j equal to 1/2 and 3/2 would appear with relative intensities 1:2, for example; the lower binding energy component being the more intense.

Satellite and plasmon loss peaks

When not using synchrotron radiation, the exciting X-ray beam is often not perfectly monochromatic but has so-called satellite peaks shifted in energy from the main spectral line (an explanation for the origin of satellites in the X-ray source is given in section 2.3.2). These satellite peaks are reflected in the XPS spectrum, since the energy of the photoelectrons depends on the photon energy (see Eq. 7). Satellite peaks are much lower in intensity than the main line and can generally be easily identified.

Another mechanism that can cause additional peaks in the spectrum for some materials is a loss of energy due to plasmon excitation. This can happen as the photohole is deexciting, in which case *intrinsic* plasmons are created. *Extrinsic* plasmons are excited somewhere else along the path of the photoelectron to the surface of the solid [28]. As these excitations are quantised they can be separated from other loss mechanisms, which simply contribute to the broad background of the photoemission spectrum. They will instead produce peaks shifted to higher binding energies from the main photoelectron lines.

2.2.3 Inverse Photoelectron Spectroscopy

Photoemission spectroscopy provides us with an effective tool to probe the occupied states of a specimen. For probing the unoccupied states Inverse Photoemission Spectroscopy (IPES) can be used. In IPES, the sample is not irradiated by photons, but by monochromatic electrons, which couple to the unoccupied states above the Fermi level. As they relax to lower unoccupied energy levels, they emit photons, whose energy can be used to determine the binding energy of the final state via

$$E_i = E_f + h\nu, \tag{10}$$

where E_i is the energy of the incoming electron and E_f is the final unoccupied state it relaxes to. The process is illustrated in Fig. 11 for a semiconductor, together with the photoemission process. The main challenge of IPES is that the inverse photoemission process has a very low yield. The ratio of the differential cross sections of the inverse photoemission and the photoemission processes is given by

$$R = \left(\frac{\lambda_e}{\lambda_{ph}}\right)^2, \tag{11}$$

where λ_e and λ_{ph} are the wavelengths of the emitted electrons and photons, respectively. In the UV range <100 eV, $R \approx 10^{-5}$ and on the order of 1000 eV (characteristic of XPS), $R \approx 10^{-3}$ [31]. The low cross section creates a need for high sensitivity photon detectors. Additionally, long measuring times may be unavoidable to obtain a strong enough signal.

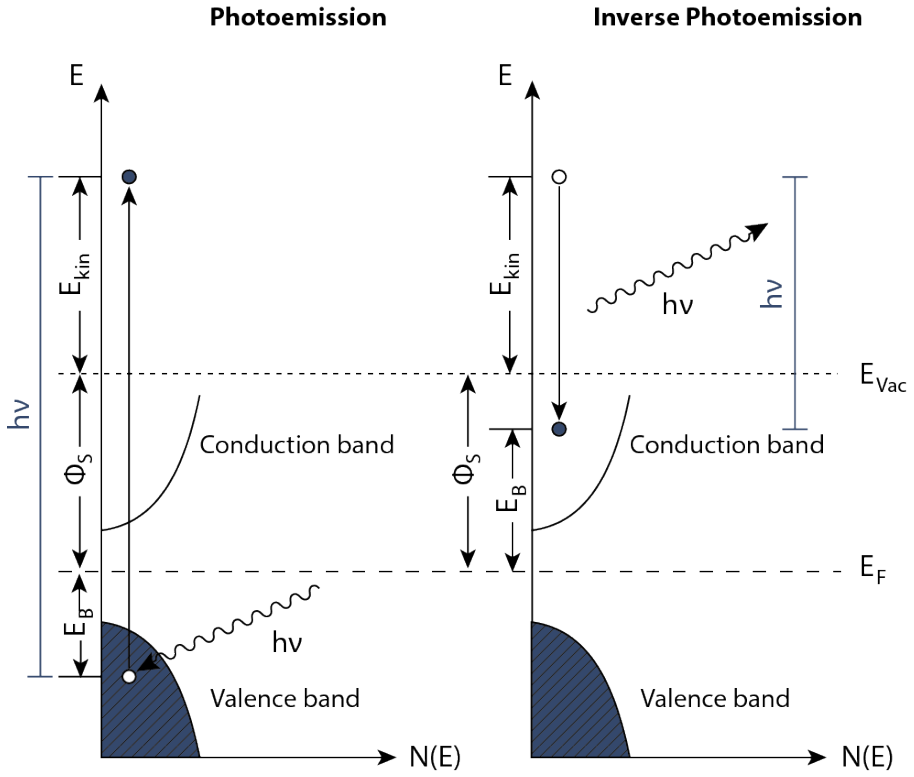

Figure 11: Illustration of the principle of inverse photoemission compared to photoemission on a semiconductor.

IPES can generally be measured in two different modes. In isochromat mode, the detected photon energy is kept constant and the energy of the electron beam is ramped. In spectrograph mode, the electron beam energy is fixed and the emitted photons are analysed with a grating spectrometer.

Combining photoemission and inverse photoemission spectroscopy measurements allows for a complete study of the electronic structure of a sample. Since both the valence band edge and the conduction band edge are known, it is thereby possible to determine the band gap of a material.

2.2.4 Surface sensitivity of PES

All PES based techniques are inherently surface sensitive as a result of the limited distance electrons can propagate in matter undisturbed. The deeper in the solid a photoelectron is created, the less likely it is to reach the surface and the detector. The key parameter determining the sampling depth is the inelastic mean free path λ of the electron, which is defined as the average distance between two scattering processes. While λ does depend on the material the electron is travelling in, it has been empirically found that it tends to follow a so-called *universal curve* that is a function of the electron energy. In Fig. 12 this curve is displayed over a relevant energy range, showing measured values for individual elements and a line indicating the theoretical prediction. The reason for the universal trend is that in this energy range the inelastic scattering is mostly due to excitations of valence band electrons, and the electron density in the valence band is very similar for most materials [32, 33]. The curve has a broad minimum at around 70 eV, where the mean free path is on the order of only a few Å. This energy regime therefore allows for probing only a few atomic layers. The dependency of λ on the electron energy can be exploited when the photon source is tunable to a desired wavelength, which generally is only the case at a synchrotron.

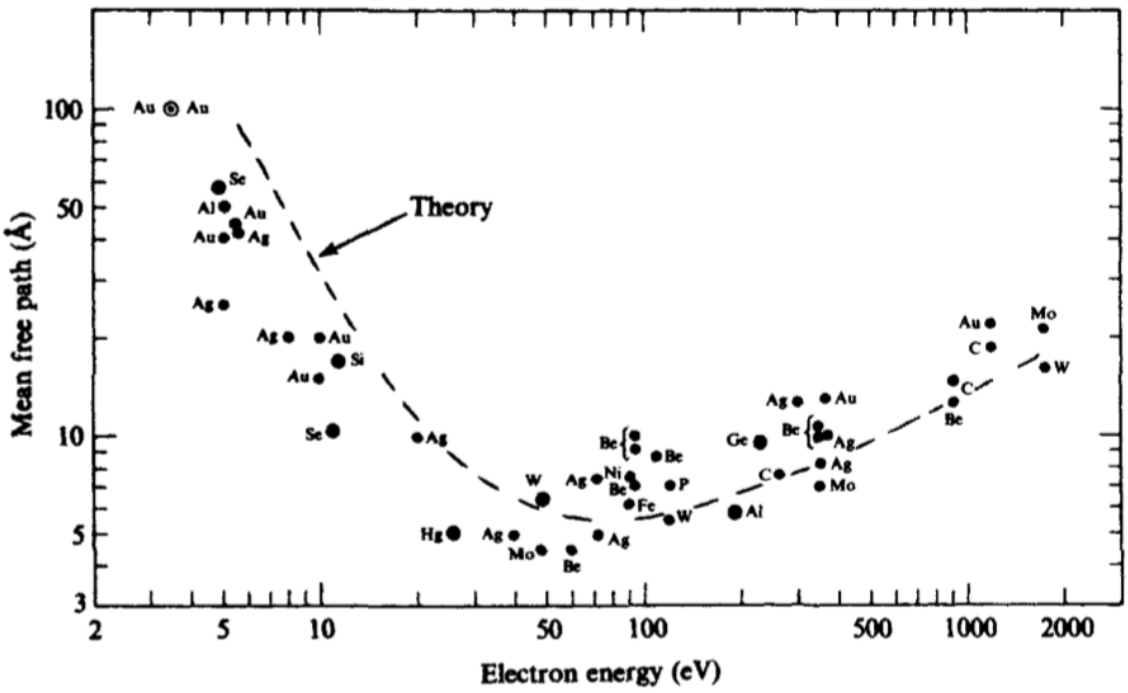

Figure 12: Electron mean free path as a function of electron energy for various elements. Adapted from reference [33].

The intensity $\mathrm{d}I$ of detected photoelectrons created at a depth of z drops exponentially according to [28]

$$\mathrm{d}I \sim e^{(-z/\lambda\cos\theta)}\mathrm{d}z, \tag{12}$$

where θ is the emission angle with respect to the surface normal. From this, the information depth is defined as the depth from which a defined percentage (e.g. 95% or 99%) of the total signal originates [34]. For XPS, this depth is often quoted as ca. 3λ, which is on

the order of a few nanometers.

The very short inelastic mean free path of electrons also creates the need to perform PES experiments in ultra-high vacuum (UHV), i.e. in the range of 10^{-9} mbar and below. This is to ensure that the sample surface is clean and remains contamination free throughout the experiment, and to avoid additional collisions of photoelectrons with gas atoms on their way to the detector.

2.3 X-ray Diffraction (XRD)[3]

X-ray diffraction is one of the most widely used techniques for structural analysis of materials. Diffraction from crystals, i.e. structures that are periodic in space, is described by Bragg's law. It states the condition for constructive interference of waves with a wavelength λ hitting a crystal, whose lattice planes are spaced at a distance d, under an angle of incidence θ (see Fig. 13) as

$$2d \sin\theta = n\lambda, \tag{13}$$

where n is an integer. Bragg's law can be used for chemical identification, as it allows for the determination of the crystal's lattice parameters. The positions of the Bragg reflections also contain information about possible macro-strain of the lattice and qualitative phase analysis, when several phases are present in the sample [38].

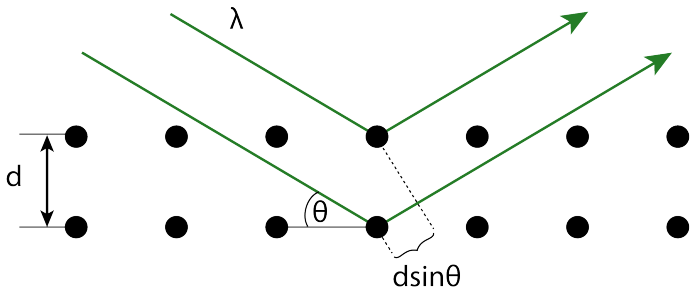

Figure 13: Illustration of the principle of Bragg diffraction. Two incoming light beams scattering off two different atoms in a crystal lattice, interfere constructively if the difference in the path length they travel is an integer multiple of their wavelength.

Apart from the positions of the peaks in a diffraction pattern, their intensities also provide information about the crystal. If the lattice vectors defining the crystal lattice are denoted by $\boldsymbol{R}_n$ and the positions of the atoms with respect to any given lattice site by $\boldsymbol{r}_j$, any atom position in the crystal is given by $\boldsymbol{R}_n + \boldsymbol{r}_j$. The intensity of the scattering for which constructive interference occurs is then given by the so-called structure factor [35],

$$F(\boldsymbol{Q}) = \underbrace{\sum_j f_j(\boldsymbol{Q}) e^{i\boldsymbol{Q}\cdot\boldsymbol{r}_j}}_{\text{Unit cell structure factor}} \underbrace{\sum_n e^{i\boldsymbol{Q}\cdot\boldsymbol{R}_n}}_{\text{Lattice sum}}, \tag{14}$$

where f_j is the atomic scattering factor, which is the Fourier transform of the electron density, and $\boldsymbol{Q}$ is the scattering vector, defined as the difference between the wavevectors of the incoming wave and the scattered wave. The first term of the equation is the structure factor stemming from the unit cell and the second term is a sum over all lattice sites in the crystal. The observed intensity in an experimentally obtained diffraction pattern is the modulus squared of the structure factor $|F(\boldsymbol{Q})|^2$. This intensity can be used to find the positions of the atoms in the unit cell. In addition to that it carries information on the occupancy of atomic sites, as well as the texture, i.e. the orientation of crystallites in a poly-crystalline sample [38].

[3]This section is based on references [35–37].

2.3.1 X-ray sources

Several different factors determine the quality of an X-ray beam produced by a source: the number of emitted photons per second, the collimation of the beam, the source area and the photon energy range, that has been conventionally defined as a fixed relative energy bandwidth (BW) often chosen to be 0.1%. To combine these aspects into one single quantity that can be used to compare X-ray sources, the **brilliance** of a source has been defined as

$$B = \frac{\text{photons/second}}{(\text{mrad}^2)(\text{mm}^2 \text{ source area})(0.1\%\text{BW})}.$$

During the second half of the twentieth century, there has been an enormous increase in brilliance of X-ray sources, as is illustrated in Fig. 14, showing the achieved relative peak brilliance over time.

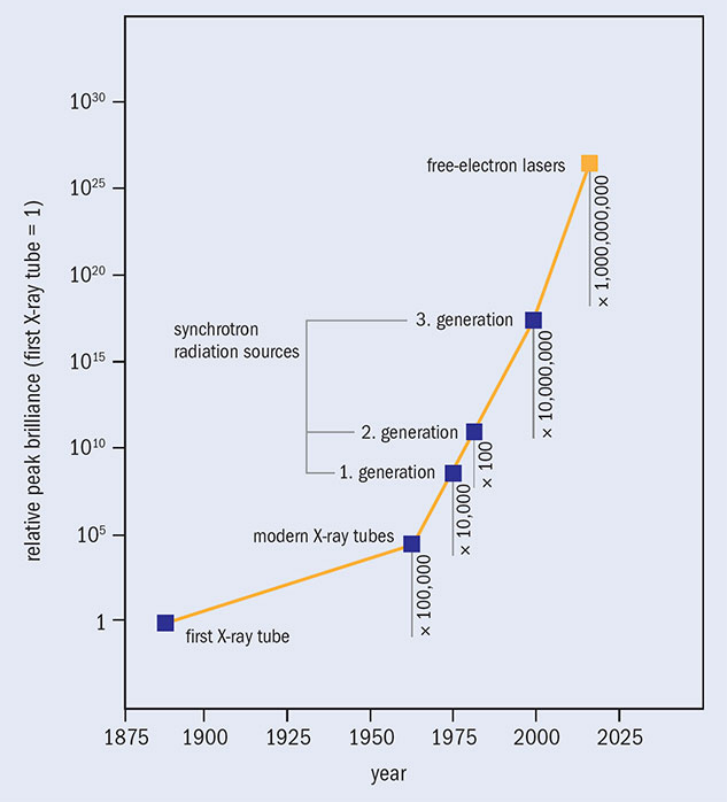

Figure 14: Plot showing the peak brilliance of X-ray sources relative to that of the first X-ray tube as a function of time since the discovery of X-rays in 1895. Adapted from reference [39].

While the standard is currently still marked by 3rd generation synchrotron radiation, a new generation of X-ray sources is on the rise with free electron lasers (FELs). These are expected to boost peak brilliance by another 10 orders of magnitude. The latest FEL facility, that was opened to user operation in September 2017, is the European X-ray free-electron laser (XFEL) in Hamburg, with a peak brilliance of $\sim 10^{33}$ photons/s/mrad^2/mm^2 /0.1%BW [40].

2.3.2 The X-ray tube

The X-ray tubes that are commonly used on a laboratory scale nowadays are still based on the tube invented by W.D. Coolidge in 1912. The working principle is illustrated in Fig. 15a. A filament is heated and emits electrons, that are then accelerated towards a water-cooled anode in a high voltage field. When the electrons hit the anode, both bremsstrahlung and X-rays characteristic of the anode material are created (see Fig. 15b). Bremsstrahlung arises from the deceleration of the electrons as they are deflected by other charged particles in the anode. It therefore forms a continuum with its maximum energy corresponding to the high voltage applied to the tube. The characteristic sharp lines in the spectrum arise from elastic interactions of the electrons with atoms in the anode. When the incoming electrons transfer their energy to a core electron, they can remove it from its shell thereby creating a vacancy. When the vacancy is subsequently filled by relaxation of a higher energy electron, X-rays with a wavelength corresponding to the difference of the energy levels involved in the transition are emitted (see Fig. 15c)).

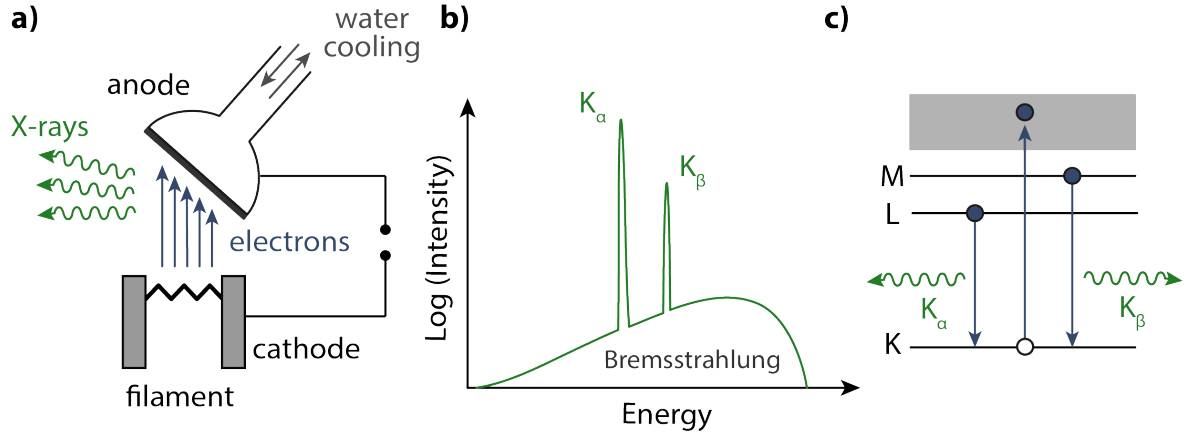

Figure 15: **a)** Schematic diagram of the X-ray tube developed by Coolidge, **b)** The spectrum of an X-ray tube shows discrete spectral lines characteristic of the anode material over a broad continuum of bremsstrahlung radiation. **c)** Schematic energy diagram illustrating the origin of the spectral lines. The K_α lines originate from transitions between the L and the K shell, while K_β lines originate from M to K shell transitions. Based on reference [35].

To obtain a monochromatic beam, the K_α line, which in the Siegbahn notation denotes the transitions from the L-shell to the K-shell, is most commonly utilised. Both the K_α and the K_β line (resulting from M to K transitions) however possess a number of satellite peaks at slightly shifted energies, which originate from simultaneously ionised shells in the atom. When a vacancy in the K-shell is filled while another vacancy is present in the L-shell (a so-called spectator hole), the total energy of the shell is shifted, leading to a K_α satellite [41]. Another effect producing satellites is the radiative Auger effect (RAE), where the K hole is filled not under emission of a full energy X-ray photon or a full-energy Auger electron, but simultaneous emission of a lower-energy photon and excitation of an electron in an outer shell [42]. As a result, a simple X-ray tube without a monochromator does not provide a perfectly monochromatic beam, even though the intensity of the satellite peaks is much lower than that of the main spectral line.
Another major drawback of the X-ray tube is that the energy of the produced X-rays is dependent on the anode materials and cannot be continuously tuned. This, and the

limitations in brilliance are the reason why in many cases an X-ray tube is not sufficient as a light source and synchrotron radiation is needed.

2.3.3 Synchrotron radiation

Synchrotron radiation facilities are the most common sources of high-brilliance X-rays nowadays. A synchrotron consists of an evacuated storage ring, in which accelerated relativistic electrons are circulating at constant energy. The ring in fact consists of a number of straight sections interconnected by bending magnets that force the particles on a curved path. Additionally, insertion devices such as wigglers or undulators are placed in the straight sections of the storage ring, which consist of a lattice of magnets forcing the particles to perform small oscillations and thereby emit radiation. A schematic of a synchrotron source is shown in Fig. 16.

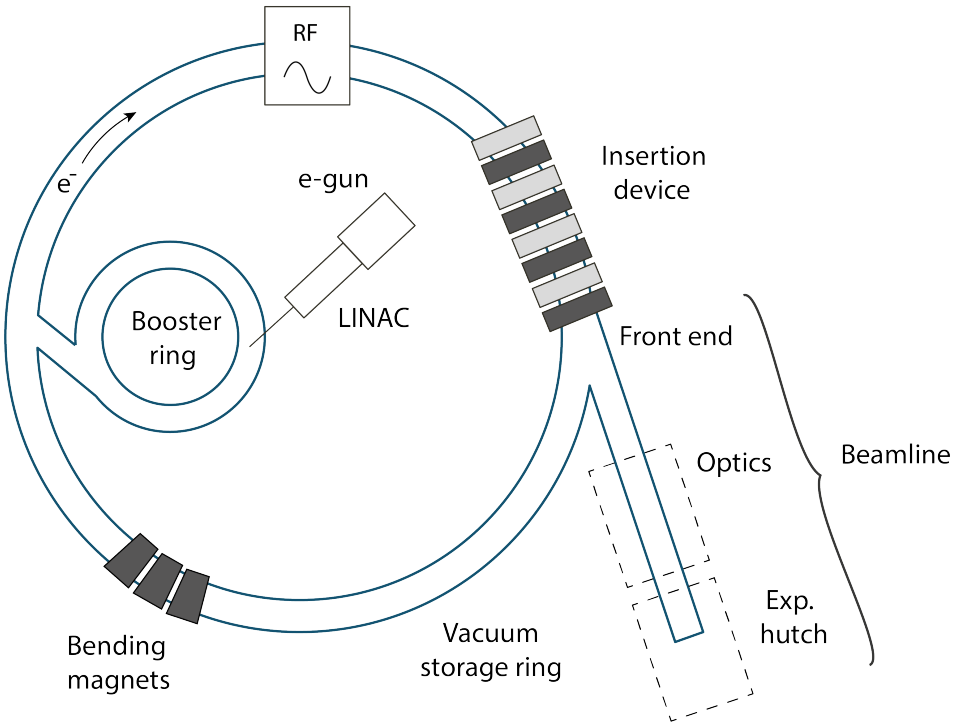

Figure 16: Schematic of a synchrotron source showing the key components. Electrons are emitted by an e-gun and accelerated by a linear accelerator into a booster ring. After further acceleration they pass on into the storage ring, where they are kept on a circular trajectory by bending magnets. Insertion devices emit X-ray radiation tangential to the storage ring forming the beamlines, where experiments are performed. A radio frequency source replenishes the energy lost by the electrons after emitting radiation. Based on reference [36].

A synchrotron possesses five key components which are:

1. The **electron source**, generating electrons by emission from a hot filament. A constant supply of electrons needs to be guaranteed, as there are always losses in the storage ring. A linear accelerator accelerates the electrons to ca. 100 MeV.

2. A **booster ring** that serves to accelerate the electrons to the energy of the electrons in the storage ring. From there they are periodically injected into the storage ring.

In modern facilities, the current is being topped up almost continuously with very small time intervals between the injections, allowing the synchrotron to be operated at essentially constant current.

3. The **storage ring** is where the electrons are travelling at highly relativistic speeds on a closed path that they are forced on by magnetic fields. In-between the bending magnets, there are straight sections in the structure of the ring where insertion devices (undulators or wigglers) are placed, to produce radiation. The bending magnets themselves can also be used to provide radiation, however with a smaller brilliance than what is achieved with insertion devices.

4. A **radio frequency cavity** is used to supply energy back to the electrons after they have emitted radiation, so that they do not deviate from their path and are lost.

5. The **beamlines** that run tangential to the storage ring is where the radiation is used for experiments in experimental hutches. Before reaching the experimental hutch the beam runs through an optics hutch where it is focused and monochromated. The so-called front end of the beam line has several functions like filtering the spectrum and separating the beamline vacuum from the storage ring vacuum.

Bending magnet radiation

A bending magnet is the simplest insertion device to produce X-rays in a synchrotron. While bending magnet radiation is not as brilliant as that created by wigglers and undulators it is still commonly used, such as for this thesis at the Brazilian Synchrotron Light Laboratory (LNLS).
When super-relativistic electrons are deflected by a magnetic field, they emit tightly collimated cones of radiation tangential to the electron trajectory, as illustrated schematically in Fig. 17a. The emitted radiation depends on two parameters, the angular frequency of the electrons ω_0 and their energy in the storage ring that is given by the Lorentz factor in units of the rest mass energy:

$$\gamma = \frac{\mathcal{E}}{mc^2}. \tag{15}$$

This determines the opening angle of the cone, which is proportional to $1/\gamma$. The emitted radiation covers a broad spectrum, but for photon energies higher than about $\gamma^3\omega_0$, the spectral intensity falls off quickly. It is therefore useful to define the characteristic or critical frequency ω_c given by

$$\omega_c = \frac{3}{2}\gamma^3\omega_0. \tag{16}$$

In practical units the critical photon energy $\hbar\omega_c$, that depends on the electron energy $\mathcal{E}$ and the magnetic field B can then be expressed as

$$\hbar\omega_c[\mathrm{keV}] = 0.665 \cdot \mathcal{E}^2[\mathrm{GeV}] \cdot B[\mathrm{T}]. \tag{17}$$

The spectral distribution of the emitted radiation is shown in Fig. 17b. It is a universal function of the ratio between the photon energy and the characteristic cut-off energy that scales with $\mathcal{E}^2$ and the current I in the storage ring. At the beamline, a slit usually selects a fan of the emitted radiation cone in the horizontal plane. The desired photon energy

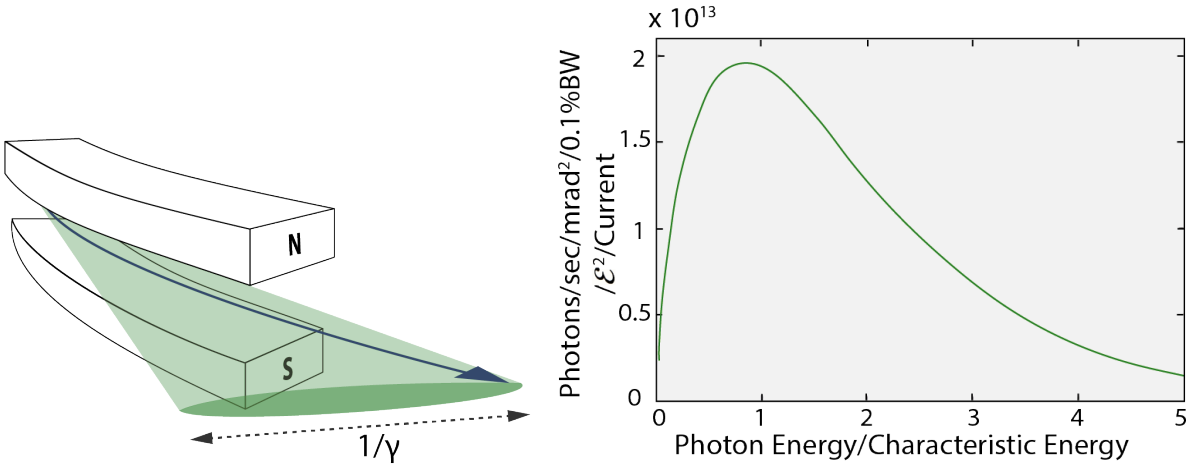

(a) (b)

Figure 17: **(a)** Schematic diagram of a bending magnet in a synchrotron indicating the electron trajectory (blue arrow) and the emitted cone of radiation (green). Based on reference [43]. **(b)** Spectrum emitted from a bending magnet, normalised by the square of the electron energy and the beam current. Based on reference [35].

is then selected from the spectrum using monochromators such as silicon, germanium or diamond crystals.

3 Experimental

3.1 Sample preparation

In this project, different techniques of sample preparation were applied in order to obtain films suitable for different experiments. These techniques are described below. The dyes used for all experiments were purchased in powder form from *Sigma-Aldrich*. Furthermore, different substrate materials were used to comply with the requirements of the specific measurements. The used substrates as well as details on the specific sample preparation are described in the corresponding section on the respective experimental method.

Solution processing

A simple and fast way of film deposition is to dissolve the molecules in a solvent, drop it onto a substrate and let the solvent dry off or degas in vacuum. For this thesis, all solution-cast samples were prepared using ethanol as the solvent. The solutions were prepared by mixing 0.018 g curcumin and 0.0013 g bixin with 1 ml ethanol, respectively, and leaving them in an ultrasonic bath for a few minutes.

Thermal evaporation

Thermally evaporated samples were prepared in the vacuum chamber using an in-house built evaporator with an integrated thermopcouple to monitor the temperature. The evaporator has a tantalum pocket, which is filled with the powder to be evaporated. After filling the evaporator and installing it on the vacuum system, it was slowly heated by passing a current through it. Before the evaporation it is necessary to allow for the degassing of water and other contaminants to obtain a pure deposition. The evaporator temperature and pressure in the chamber were carefully monitored during the degassing, since the exact boiling point of curcumin and bixin under vacuum conditions was not known. The evaporator was placed as closely to the sample as possible to maximise the deposition rate.
Thermal evaporation has many advantages compared to solution processing, like nanometer control of the film thickness and high uniformity. Additionally, it has the potential of creating films with a higher intermolecular degree of order [44]. However, many organic molecules are known to degrade during the evaporation/sublimation process [45].

3.2 Ultraviolet–Visible spectroscopy (UV-Vis)

UV-Vis measurements were performed in order to measure the absorption spectra of the deposited films. The main motivation for these measurements was to check whether the molecules change under thermal evaporation, i.e. if they polymerise. The spectrophotometer used for these experiments was an *Olis* 14. The basic setup of such an instrument is shown in Fig. 18. Two different light sources are available, a deuterium lamp for UV light and a tungsten lamp for visible and NIR light. Together, these span a measurable wavelength range of 185-2600 nm. For the experiment, a desired wavelength range is selected, across which the instrument scans the probe beam by using a filter and a monochromator. The beam is split between the sample and a reference. Behind each, the photon intensity is measured by a photomultiplier throughout the UV and visible region and by a lead sulfide (PbS) detector throughout near-infrared (NIR). The signals are then processed to

produce the absorbance or transmittance of the sample over the selected wavelength range.

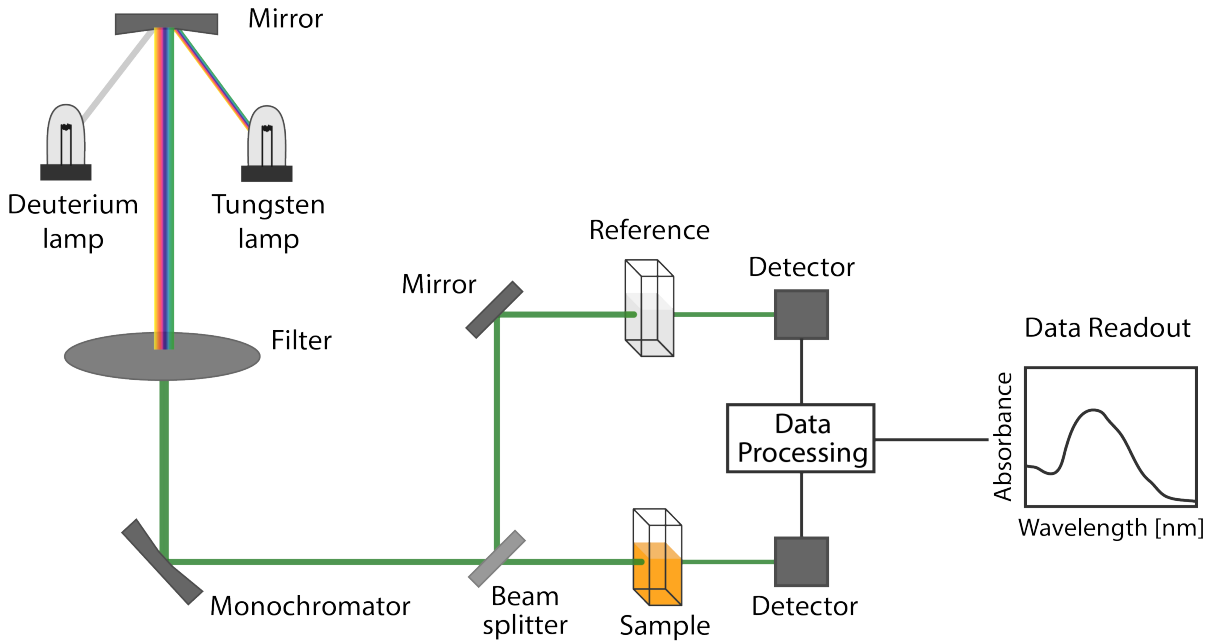

Figure 18: Schematic diagram of a UV-Vis spectrophotometer. Based on reference [46].

Before each measurement, a baseline scan was taken without any sample inserted in the instrument. This baseline was subtracted from all subsequent measurements. The samples were prepared by evaporating the dyes onto 1 mm thick quartz glass holders, as quartz has very low absorbance in the wavelength range of interest (ca. 300 - 700 nm). To verify this, a spectrum of a clean quartz glass holder was measured.

3.3 Photoelectron Spectroscopy (PES)

3.3.1 Vacuum System[4]

A (simplified) schematic diagram of the vacuum system used in this thesis for photoemission measurements to study the electronic structure of the dyes is shown in Fig. 19. The system consists of three chambers: a load lock, a preparation chamber, and the analysis or main chamber. The load lock is a small chamber that can quickly be vented and pumped down again to a medium-high vacuum to insert samples into the system. For this thesis, a thermal evaporator for sample preparation was also mounted on the load lock. The preparation chamber can be used for different kinds of sample preparations, but was not used in this thesis. The analysis chamber is where all photoemission experiments took place.

To obtain ultra-high vacuum (lower than 1×10^{-9} mbar), which is required for photoemission spectroscopy, the chambers are evacuated by a system of pumps.
Rotary vane pumps are used to establish a "rough vacuum" on the order of 10^{-3} mbar, which is why they are also referred to as roughing pumps. Creating a rough vacuum is

[4]This section is based on references [47, 48].

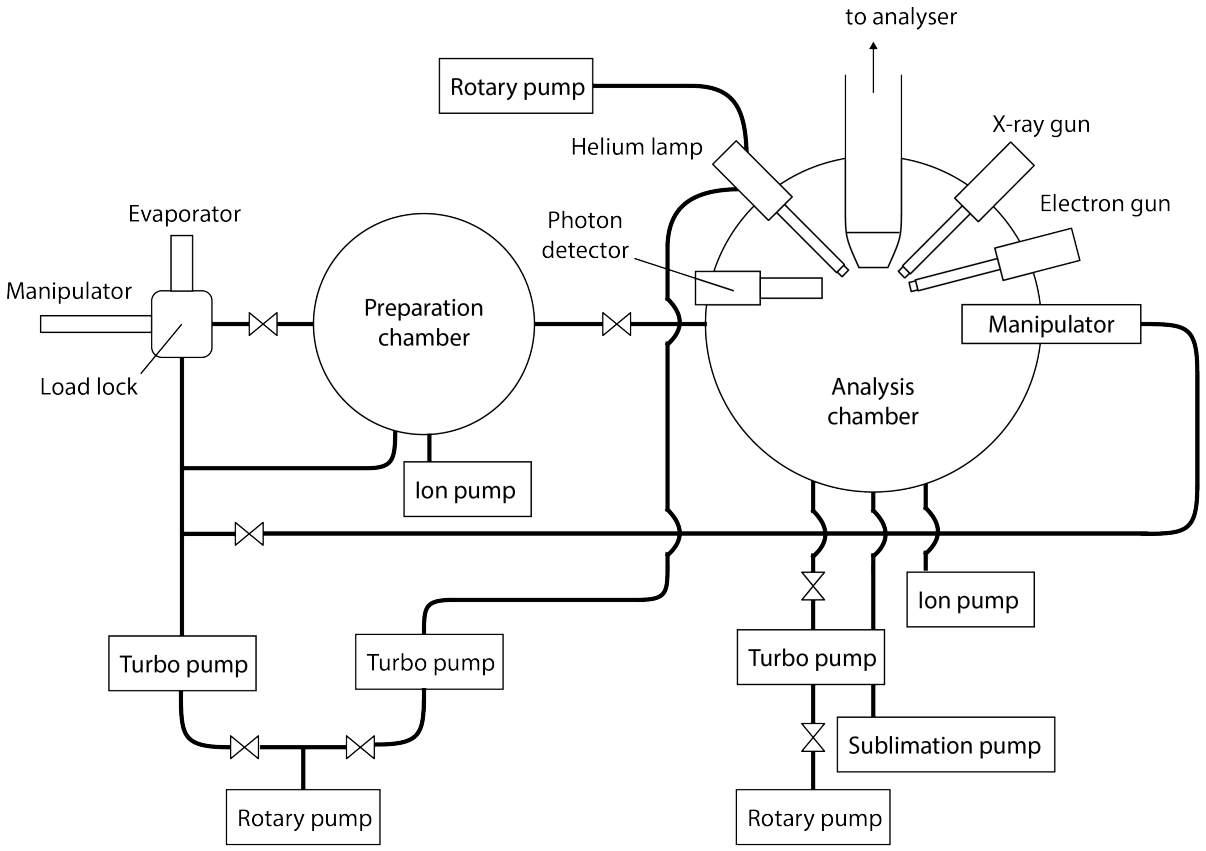

Figure 19: Simplified schematic diagram of the vacuum system used for photoemission spectroscopy.

necessary for pumps operating in the higher vacuum regimes to run efficiently. Rotary vane pumps are positive displacement pumps, which operate by repeatedly enclosing a gas volume from the chamber and forcing it into the exhaust pipe. In the current setup, one rotary pump is used to pump the load lock and the preparation chamber and another one to pump the analysis chamber. An additional rotary pump is connected to the helium lamp used in UPS (see section 3.3.2).
To obtain vacuum up to around 1×10^{-10} mbar, turbomolecular pumps are used. These operate in the molecular flow regime, where gas atoms are more likely to collide with the chamber walls than with other gas atoms. They use a turbine with rapidly rotating blades that transfer their momentum to the gas atoms forcing them in a desired direction. Turbomolecular pumps cannot operate in the laminar flow range, where gas atoms frequently collide with each other (typically $> 10^{-3}$ mbar). This creates the need to back them by an adequate roughing pump. The system uses three turbomolecular pumps, one exclusively connected to the analysis chamber, one connected to the load lock, ion pump and the manipulator of the analysis chamber, and the third one to the helium lamp.
Both the preparation chamber and the analysis chamber are additionally pumped by an ion pump. This is a type of capture pump that does not exhaust the gas atoms but traps them in itself. Using strong electric fields, the gas atoms are ionised and accelerated towards a solid electrode where they are captured.
Another type of capture pump is the titanium sublimation pump, which is used for additional pumping in the analysis chamber, as this is where the highest vacuum is required. This pump sublimates the chamber walls with titanium ions from a filament. As titanium

is very reactive, it forms solid compounds with gas atoms colliding with the wall, thereby further reducing the pressure in the chamber.

For all photoemission experiments, samples were prepared on molybdenum disulfide (MoS_2) substrate. This substrate is chosen for several reasons. It is conductive, which is important to avoid charging of the sample during the measurements. It does not easily oxidise and, since it is a layered material, it can be cleaved whereby a clean surface can easily be obtained. For minimum contamination this is done just before the sample is put into vacuum.
The molybdenum disulfide was glued onto the sample holder using a conductive two-part silver epoxy adhesive that hardens upon heating. After the molybdenum disulfide was cleaved, the dyes were deposited either by drop-casting of solutions onto the substrate and subsequent degassing of the solvent in the vacuum chamber, or by thermal evaporation inside the vacuum chamber. Tab. 1 gives an overview of the process parameters of the samples prepared for photoemission experiments. The high availability of curcumin allowed for trying out variations in the duration and temperature of the thermal evaporation. In the case of bixin on the other hand, the thermal evaporation was simply continued until a drop in the chamber pressure indicated that all powder had evaporated from the evaporator.

Table 1: Process parameters for the samples prepared for photoemission experiments. The substrate material in all cases was molybdenum disulfide.

Curcumin		Bixin	
Evaporated	Solution-cast	Evaporated	Solution-cast
15 min @ 170°C		∼60 min @ 170°C	ethanol
135 min @ 170°C			
60 min @ 220°C			

3.3.2 Ultraviolet Photoelectron Spectroscopy (UPS)

UPS was performed using the UVS 10/35 UV discharge lamp from *SPECS*. While it can be operated with a variety of gases, in this project only helium was used. Through a gas inlet, a quartz capillary is filled with the gas, where a discharge is ignited. This creates a plasma, which emits UV light at wavelengths characteristic of the operating gas. In the case of helium these are most importantly the HeI_α line at 21.22 eV and the $HeII_\alpha$ line at 40.82 eV. The light is guided through a beam guide capillary into the analysis chamber. In order to directly connect the lamp to UHV on a windowless path, there are two stages of differential pumping. The first stage is evacuated by a rotary pump and the second stage by a turbo pump. To prevent the lamp from overheating, it is cooled by a fan.
Since the HeI_α radiation originates from unionised He atoms and the $HeII_\alpha$ radiation from singly ionised ones, the lines can be selected by adjusting the gas pressure in the discharge capillary. When the pressure is lower, electrons in the plasma have a longer mean free path and can therefore be accelerated to higher speeds, thereby ionising more of the helium gas. Therefore, the $HeII_\alpha$ portion increases with regards to HeI_α as the pressure is reduced. In this thesis, all measurements were done using the HeI_α line, which was obtained by operating the lamp at a stable pressure of 5×10^{-8} mbar.

The spot size of the UV lamp on the sample is ca. 2.2 mm. So, in order to probe a larger area of the sample, several different positions were measured. Furthermore, the sample is connected to ground in order to replenish the emitted electrons and avoid charging, as this can lead to shifts in the spectrum.

3.3.3 X-ray Photoelectron Spectroscopy (XPS)

The XPS system uses an XR-50 gun from *SPECS*. It is an unmonochromated source with a magnesium/aluminium twin anode. In this thesis, all measurements were done using the magnesium anode, whose $K_{\alpha 1/2}$ radiation line lies at 1253.6 eV. Its line width, according to the manufacturer, is 680 meV. Since the source is not monochromated it also produces satellite lines, most importantly the $MgK_{\alpha 3}$ shifted by 8.4 eV from the main line. An aluminium window is placed at the exit of the gun to attenuate the signal such that only the most intense part of the spectrum is transmitted, thereby eliminating the bremsstrahlung contribution.

For performing XPS, the X-ray gun is moved close to the sample. The titanium sublimation pump is turned off to maintain UHV at all times during the measurement. Like in UPS, the sample in grounded to keep it from charging.
Initial widescans were performed on all samples. This is to obtain an overview over the entire spectrum in order to be able to determine which elements are present in the sample. It also allows for checking if the sample is properly positioned such that the X-ray beam exclusively hits the sample and not the sample holder. This is most easily done by checking the spectrum for iron peaks. In addition to the widescans, high resolution spectra of the C1s and the O1s core levels were measured, as the samples are composed of carbon and oxygen. On some samples, high resolution scans of the Mo3d line stemming from the molybdenum disulfide substrate were measured, since their intensity can be used to estimate the film thickness.

3.3.4 Inverse Photoemission Spectroscopy (IPES)

Isochromat IPES was performed using a system by *PSP Vacuum Technology*. The electron beam in the gun is produced by thermionic emission from an indirectly heated barioum oxide (BaO) cathode. Barium oxide has a low working temperature (between 1100 K to 1200 K), which is important to achieve a low energy spread (ca. 0.25 eV (FWHM)), which ultimately determines the energy resolution of the system [49]. It also has a low work function (ca. 2 eV), which is desirable in order to achieve a high electron emission to make up for low counting rates of the photons [50]. The electron gun produces a low energy electron beam in the range 5 to 50 eV.

The emitted photons are detected by a bandpass detector that is designed such that only photons of a specific energy are detected (9.5±0.5 eV). This is achieved by making the photons pass through a strontium fluoride (SrF_2) window, whose transmission has a sharp cutoff above the desired photon energy. The window thereby filters out the photons with too high energy. They then hit a sodium chloride (NaCl) coated photocathode whose photoionisation efficiency sets in just near the desired photon energy, filtering out those photons whose energy is too low. The absorption of photons in the sodium chloride layer leads to the emission of electrons, which are multiplied in a channeltron.

3.3.5 Data Analysis

XPS peak fitting

All XPS peaks were fitted in Matlab with a Pseudo-Voigt function made up by the sum of a Lorentzian and a Gaussian function [51],

$$\text{Pseudo-Voigt} = (1-m)\sqrt{\frac{4\ln(2)}{\pi{\omega_G}^2}}\exp\left[-\left(\frac{4\ln(2)}{{\omega_G}^2}\right)x^2\right] + \frac{m}{2\pi}\frac{\omega_L}{\frac{{\omega_L}^2}{2}+4x^2}, \tag{18}$$

where $x = (E - E_0)$, ω_G is the FWHM of the Gaussian, ω_L is the FWHM of the Lorentzian and m is a parameter controlling the relative weighting of the two functions. This convolution of lineshapes is necessary as there are a number of sources for peak broadening that have different profiles. The Lorentzian broadening originates partly from the finite lifetime of the core hole state. Additionally, the broadening caused by the used X-ray source is assumed to be Lorentzian (as opposed to a Gaussian broadening of synchrotron sources). Since this broadening is much bigger than that originating from the core hole lifetime, the effect of the latter is negligible. The Gaussian broadening is caused by atomic vibrations as well as electron scattering and detection in the spectrometer [52]. Therefore both lineshapes have a contribution from the instrumentation as well as the sample.
The background originating from inelastically scattered electrons was fitted with a Shirley background that assumes a constant energy-loss function. Details can be found in reference [53].

Film thickness estimation

Due to its extremely high surface sensitivity, XPS can also be used for the measurement of film thickness. There are several different methods for doing this, the simplest of which makes use of the attenuation of the photoelectron intensity of the substrate that the film is deposited on [54]. The probability that an electron excited at a depth z leaves the sample without being scattered, decreases exponentially with the distance l it has to travel to reach the surface (see Fig. 20):

$$P(z) = e^{-l/\lambda} = e^{-z/(\lambda\cos(\theta))} \tag{19}$$

where θ is the emission angle with respect to the surface normal and λ is the inelastic mean free path of the electron, which depends on its kinetic energy (c.f. Fig. 12).

In the used setup the sample is aligned such that the emission angle is normal to the surface giving $\cos(90°) = 1$. The intensity I_S of the photoemission signal considering only the substrate without the film can then be determined by integrating over $P(z)$ [55]:

$$I_S = s_S \int_0^\infty e^{(-z/\lambda)}\mathrm{d}z = s_S\lambda, \tag{20}$$

where $s_S = \sigma_S \cdot L_S \cdot N_S \cdot \lambda_S \cdot \cos(\theta) \cdot Q(E_S)$ is an element and instrument specific sensitivity factor. σ_S is the photoelectron cross-section in cm^2, L_S is the angular asymmetry of the photoemission intensity for each atom, N_S is the atomic density in atoms/nm^3 and $Q(E_S)$ is the intensity/energy response function of the spectrometer at the kinetic energy

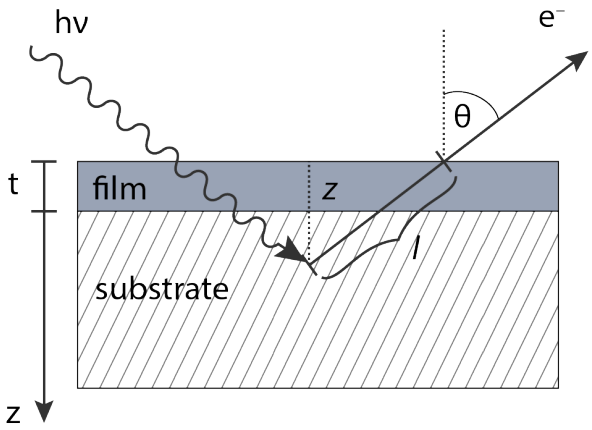

Figure 20: Schematic illustrating considerations for film thickness measurements by the overlayer attenuation method. Based on reference [30].

of the photoelectrons of the considered line.

The corresponding expression for the intensity of the signal from the film I_F is given by

$$I_F = s_F \int_0^t e^{(-z/\lambda)} \mathrm{d}z = s_F \lambda \left(1 - e^{(-t/\lambda)}\right), \tag{21}$$

where t is the film thickness. Considering the same element line in both materials, the film thickness is found from Eq. 20 and 21 to be

$$t = \lambda \ln\left(1 + \frac{I_F/s_F}{I_S/s_S}\right). \tag{22}$$

The equation can be further simplified by assuming $s_S = s_F = s$. This is clearly a crude approximation, but in many cases provides a sufficient estimate of the film thickness, which is then given by

$$t = \lambda \ln\left(\frac{I_F}{I_S}\right). \tag{23}$$

In this thesis, the inelastic mean free path was calculated using the TPP-2M formula, that was empirically derived by Tanuma et al. [56].

3.4 X-ray Diffraction (XRD)

The XRD measurements were performed at the Brazilian Synchrotron Light Laboratory (Laboratório Nacional de Luz Síncrotron – LNLS) in Campinas, Brazil. The used beamline (XRD2) is dedicated to X-ray diffraction in the hard X-ray regime (3 to 17 keV). A schematic of the beamline setup is shown in Fig. 21. The entire length of the beamline from the bending magnet to the sample covers 17.5 m. The front end of the beamline isolating the storage ring vacuum from the beamline vacuum is located at 4.8 m from the bending magnet. The X-ray beam first enters the optical hutch, where it passes through white beam slits, and is then collimated by a rhodium-coated vertical-focusing mirror and monochromated by a silicon (111) double-crystal monochromator.

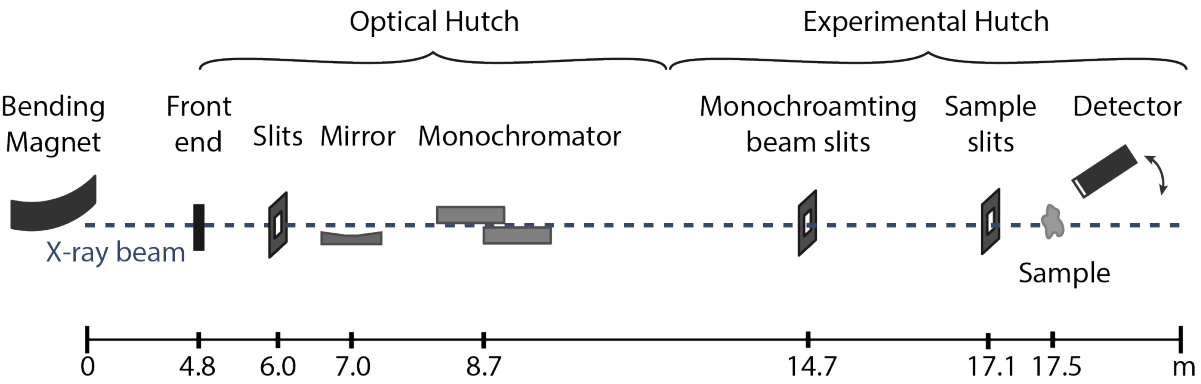

Figure 21: Schematic of the XRD2 beamline at LNLS.

Before hitting the sample, the beam passes through additional slits in the experimental hutch. The sample sits on a goniometer that allows for careful adjustment of its position. The signal is detected by a linear Mythen 1k detector by *Dectris* sitting at a distance of 91.6 cm from the sample. It has 1280 pixels with a pixel size of 50 µm and a frame rate of 2kHz.

Fig. 22 shows photographs of the beamline setup. The sample is placed on a copper sample holder with a hole (see Fig. 22a), as all measurements are performed in transmission mode. A beamstop located right behind the sample blocks the direct beam so that it does not damage the detector at small measuring angles. When the beam hits the sample, the scattered signal is recorded by the detector scanning an angular range from 3° to 30° in steps of 0.25° (see Fig. 22b). The beam energy is 8.00 keV, which corresponds to a wavelength of 1.55 Å.

Evaporated XRD samples were prepared on 1.5 µm thin aluminium foil that was spanned across a steel washer and attached to it using silver epoxy. Solution-cast samples were deposited on mylar foil. The solvent used in this case was chloroform. For the measurements, the samples where attached to the sample holder using clips. Additionally, measurements were performed on the pure unprocessed dye powders. For these, the powder was directly filled into the hole of the copper holder, which was closed on one side with 1.5 µm thin aluminium foil.
Alongside determining the crystal structures of the dyes, one of the main interests of the XRD experiment was to compare the degree of crystalline order of the different deposition techniques. A high degree of crystalline order corresponds to a low amount of trap sites where charge carriers recombine and is therefore favourable for solar cell materials. In order to investigate the influence of heat on the crystalline structure, samples were annealed on a hot plate and measured after cooling down.

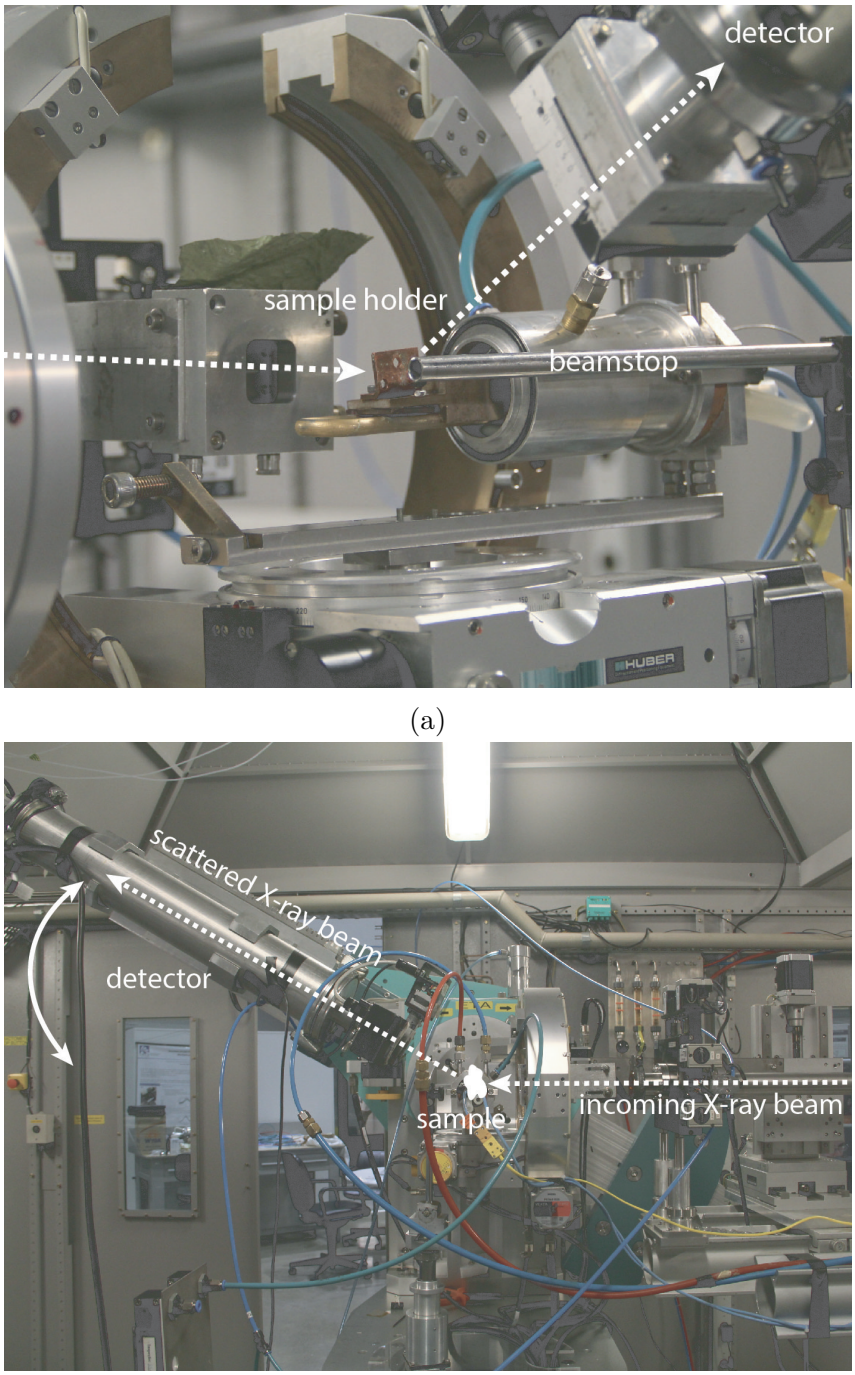

Figure 22: **(a)** Close-up photograph of the sample stage at the beamline **(b)** Photograph of the beamline indicating the trajectory of the X-ray beam and main components.

4 Results and Discussion

In this section the main experimental results will be presented and discussed. First, absorption spectra from UV-Vis spectroscopy are presented, then the results of the different PES techniques, and finally, XRD patterns measured at LNLS in Campinas.

4.1 Absorption Spectra

Absorption spectra of evaporated curcumin and bixin were measured in order to investigate if evaporation changes the structure of the molecules. If this is the case, the absorption behaviour of the evaporated films is expected to differ from that of undamaged molecules. The photograph in Fig. 23 shows the evaporated films on quartz glass substrate that the UV-Vis measurements were carried out on. Sample a) is the curcumin sample and sample b) the bixin sample. The curcumin film is visibly thicker, as only small amounts of bixin were available. To the naked eye, the curcumin film appears a similar shade of yellow as the powder it was evaporated from. The evaporated bixin film also appears rather yellow, while the powder was dark red.

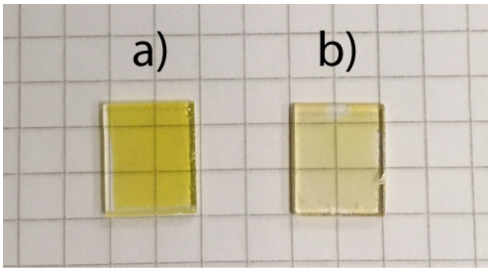

Figure 23: Photograph of thermally evaporated **a)** curcumin and **b)** bixin films on quartz glass used in UV-Vis measurements.

A clean quartz glass plate without any dye was measured to check whether its absorption behaviour interferes with that of the dyes. The spectrum is shown in Fig. 24. As can be seen, the absorbance of the plate sets in only in the UV range $< 300\,\text{nm}$. At higher wavelengths it is almost constant and negligibly small (ca. 0.05) compared to the absorbance measured on the dye films. It is therefore assumed to only cause a small constant vertical shift in the spectra measured on the dyes, which does not obstruct their interpretation.

The UV-Vis spectra measured on the two samples are presented in Fig. 25, together with spectra measured in solution and on solution-cast samples by Vilany Santana from Universidade de Brasília [57], to serve as comparison. The solvent used in those measurements was chloroform. The data was normalised in order to better compare spectral absorbance independent of film thickness. The AM 1.5 solar spectral irradiance is displayed in the background (data from reference [58]).
It can be seen that the absorption spectrum of the evaporated curcumin sample is very similar to that of the solution-cast sample with the peak position at 434 nm. This is in relatively good agreement with absorbance spectra reported in the literature (measured in methanolic-aqueous solution) [59, 60]. The peak of the in-solution spectrum is slightly shifted to shorter wavelengths.
The bixin samples, on the other hand, all exhibit very different absorption behaviour. The evaporated sample absorbs only at less than ca. 470 nm, which is in agreement with

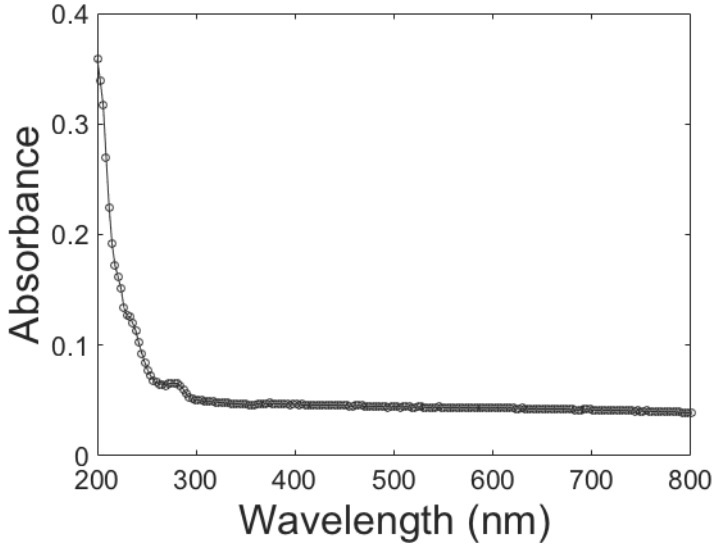

Figure 24: Absorbance spectrum of the quartz glass plate used as a substrate for the UV-Vis measurements.

its yellow colour as seen in Fig. 23. Absorption peaks at 429 nm, 457 nm and 487 nm reported in references [61, 62] (measured in acetone solution) are not observed in either of the spectra, however the agreement between the in-solution spectrum and the measurement reported in reference [10] is very good.
The fact that the in-solution spectra for both curcumin and bixin are shifted to shorter wavelengths with respect to the solution-cast spectra can likely be explained by the dissolution of dye aggregates in the solution. According to Scheibe et al. who first observed and explained this phenomenon, supramolecular polymerisation changes the absorption spectrum relative to that of the monomer by the *vicinity effect* of the adjacent molecules [63]. In this case, this causes a shift to longer wavelengths, known as a hypsochromical shift [64]. The shift strongly depends on the solvent, as explicitly illustrated for bixin in reference [65], which explains the disagreement between the measurement and the cited literature.

The absorption spectra of the molecules allow for estimation of their band gaps according to Eq. 2. The size of the band gap is limited by the maximum wavelength that is absorbed, as light of longer wavelength is less energetic. The maximum wavelength at which the molecules absorb was determined by placing a linear fit on the absorption edge and finding the intersection with the x-axis. The obtained absorption edge wavelengths together with the resulting band gaps are listed in Tab. 2. The strong shift of the absorption edge of the evaporated bixin film towards shorter wavelengths corresponds to an increased band gap as compared to the solution-cast and the in-solution sample. As a larger band gap can generally be associated with a shorter conjugation length this could be an indicator that the evaporation caused the long conjugated chain of the molecule (see Fig. 1) to break apart.

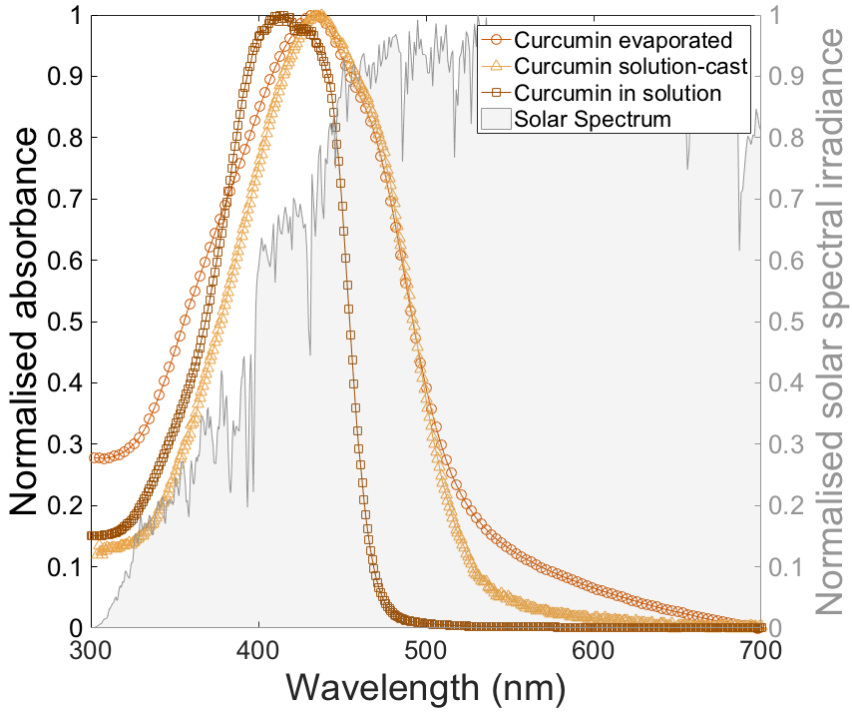

(a) Curcumin

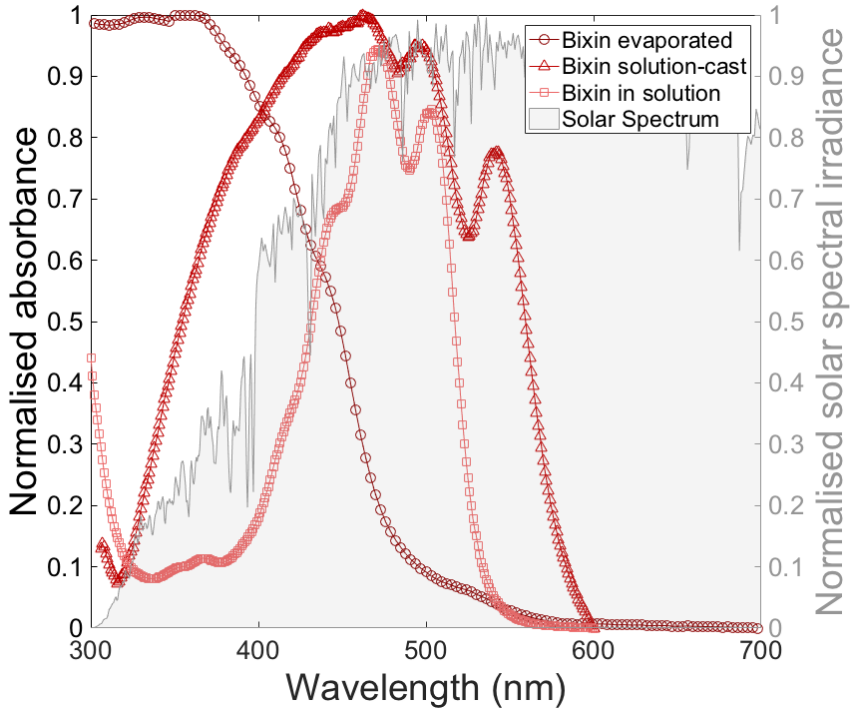

(b) Bixin

Figure 25: Normalised absorbance spectra of curcumin and bixin measured by UV-Vis displayed together with the normalised solar spectral irradiance. The different curves represent different samples that were prepared by evaporation and solution-casting as well as a sample that was measured in solution. The data of the latter two spectra was provided by Vilany Santana from Universidade de Brasília.

It should be noted that the absorbance of the evaporated bixin sample was much lower than that of the other samples due to the film being very thin. For weakly absorbing sam-

ples, the measurement error of the instrument is higher. Additionally, the fact that the cut-off of the absorption edge is less clear than on the other samples introduces a source of uncertainty when performing the linear fit. Hence, the error range of the obtained band gap for the evaporated bixin sample is assumed to be larger than that of the other samples.

Table 2: Summary of the band gap estimation from UV-Vis absorption spectra of curcumin and bixin.

	Absorption edge [nm]	Band gap [eV]
Curcumin		
Evaporated	529	2.3
Solution-cast	525	2.4
In solution	470	2.6
Bixin		
Evaporated	488	2.5
Solution-cast	582	2.1
In solution	531	2.3

From these results it is concluded that curcumin films can be prepared by thermal evaporation without chemical decomposition of the molecule. Bixin, on the other, hand seems to be more sensitive to high temperature. While this may limit its processability, it should be noted that in most applications solution-processing is generally preferred over thermal evaporation, because of cost and time factors. This result does, however, impact the interpretation of photoemission measurements performed on evaporated bixin films (see section 4.2).

4.2 Electronic Structure

In this section, the results of the photoemission measurements will be presented and discussed.

4.2.1 Film growth

Thermal evaporation

In a first electronic characterisation of the films, XPS widescans covering an energy range of 0 to 1100 eV binding energy were performed to obtain an overview over the photoemission spectra of the samples. The results are shown in Fig. 26. The four different curves represent four different samples: the freshly cleaved molybdenum disulfide substrate before evaporation (shown for comparison), the curcumin sample that was evaporated for 135 min at 170°C, the curcumin sample evaporated for 60 min at 220°C and the evaporated bixin sample. The spectrum of the curcumin sample evaporated for 15 min at 170°C showed no difference to that of the sample evaporated for 135 min at the same temperature and is therefore omitted here.

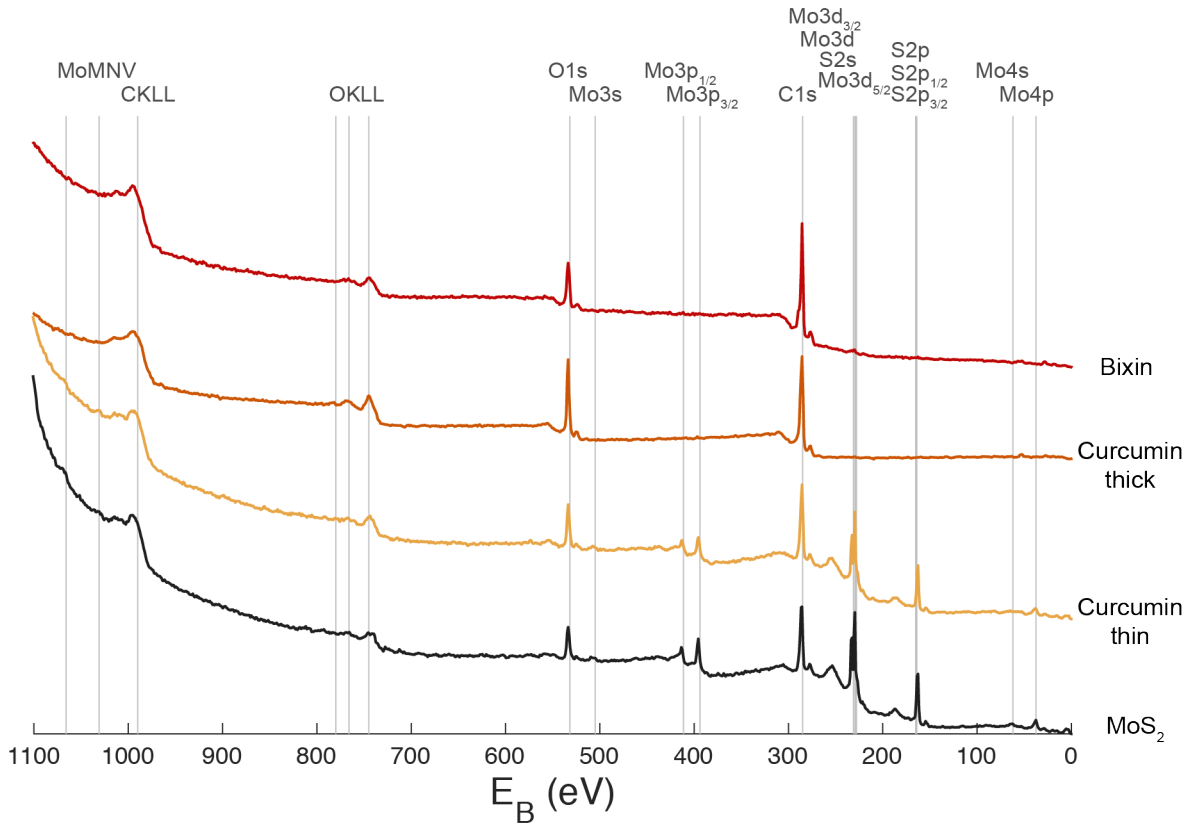

Figure 26: XPS widescans measured on cleaved molybdenum disulfide substrate, a thin and a thick evaporated curcumin film (evaporated for 135 min at 170°C and 60 min at 220°C, respectively) and a bixin film. The spectra were shifted vertically for clarity. Photoelectron and Auger lines of C, O, Mo and S are indicated.

The grey lines indicate the positions of photoelectron and Auger lines of all present elements – carbon, oxygen, molybdenum and sulphur – taken from literature [66]. The photoelectron lines are labelled according to the energy levels they arise from and the

Auger lines according to the shells involved in the transition that produced them. The small peaks at ca. 187 eV and 254 eV were identified as plasmon loss peaks of the Mo3d and S2p lines.
The main photoelectron lines observed in all spectra are the C1s and O1s lines. Even on the cleaved molybdenum disulfide these are present as a result of contamination. Additionally, on the molybdenum disulfide sample and the curcumin sample evaporated at 170°C the lines of the Mo3d- and S2p-families can clearly be seen. This is an indication that the curcumin sample evaporated at the lower temperature is very thin, despite a longer duration of the evaporation. The film on the other curcumin sample is thick enough to eliminate XPS signal from the molybdenum disulfide substrate.
High resolution spectra of the Mo3d lines on the thin curcumin (135 min at 170°C) and bixin sample are seen in Fig. 27. Fig. 27b reveals that that there is still a small contribution from the substrate present on the bixin sample, which is not visible in the widescan. The intensity difference between the Mo3d line at 230 eV measured on the samples before and after evaporation was used to estimate the thickness of the films according to Eq. 20. For a rough estimation it is sufficient to determine the intensity as the number of counts at the peak. The results are shown in Tab. 3 along with the inelastic mean free path used in the calculation, which was very similar for both materials.

Table 3: Results of the film thickness estimation on the thin curcumin (evaporated for 135 min at 170°C) and the bixin film.

	IMFP λ [Å]	thickness t [nm]
Curcumin thin	29.3	0.8
Bixin	29.1	7.2

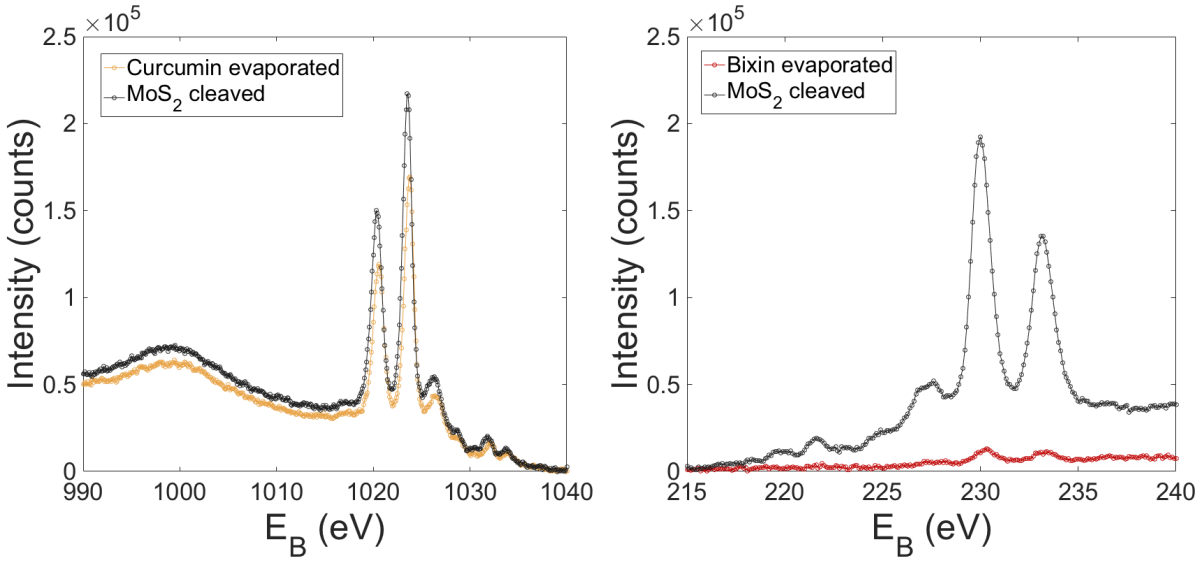

(a) Curcumin thin (b) Bixin

Figure 27: XPS spectra of the Mo3d line of the thin evaporated curcumin film and the bixin film that were used to calculate film thicknesses.

The widescans in Fig. 26 also exhibit differences in the intensity of the C1s and the O1s peaks between the dye films and the substrate. These are investigated more closely in

Fig. 28 (curcumin) and Fig. 29 (bixin), which show background-subtracted high resolution spectra of the two photoelectron lines. In addition to the samples shown in the widescan, the curcumin film evaporated for 15 min at 170°C is also included in Fig. 28. A satellite peak arising from the $K_{\alpha 3}$ line of the magnesium anode of the X-ray source can be seen at an energy shift of -8.4 eV. The photoemission lines are compared to those measured on molybdenum disulfide before evaporation. All measurements were taken on the same sample which was recleaved between evaporation at 170°C and 220°C.
The evolution of the C1s peak with increasing film thickness shows a gradual shift towards lower binding energies. A significant change in intensity with respect to the bare molybdenum disulfide is only observed for the thick curcumin sample evaporated at 220°C. That film also exhibits a shoulder on the high binding energy side of the peak, indicating the existence of different components.
For the O1s line, no shift in peak position is observed as the curcumin film is grown onto the substrate, but a clear increase in peak intensity. It is also found that the peak intensity is higher after recleaving the substrate than on the original bare substrate. An explanation for this could be that the curcumin film was not entirely removed when the sample was recleaved. It can also be seen that the peak of the thick evaporated film has a soft shoulder on the low binding energy side around 532 eV that cannot be observed on the thinner films.

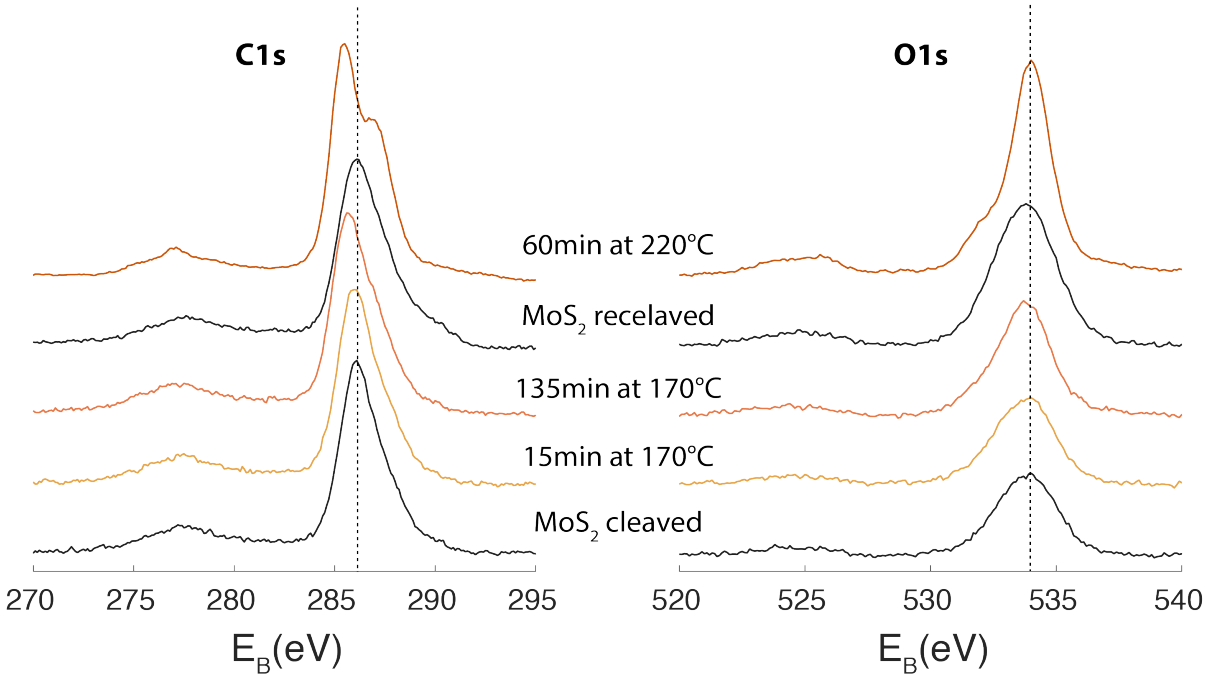

Figure 28: High resolution XPS spectra of the C1s and O1s line of curcumin showing the evolution of peak position and intensity as the film thickness increases.

The obtained results suggest that only the curcumin film evaporated at 220° is thick enough to study the molecule without contributions from organic contaminants present on the substrate. They also show that the deposition rate of the thermal evaporation is much higher at higher temperatures.

The corresponding high resolution scans of the C1s and O1s line before and after evaporation of bixin are shown in Fig. 29. On the bixin film the C1s peak shifts to lower

binding energies and reveals an additional smaller peak near 290 eV. The O1s peak shows no change in intensity, but appears to shift slightly towards higher binding energies and reveal an additional component on the low binding energy side.

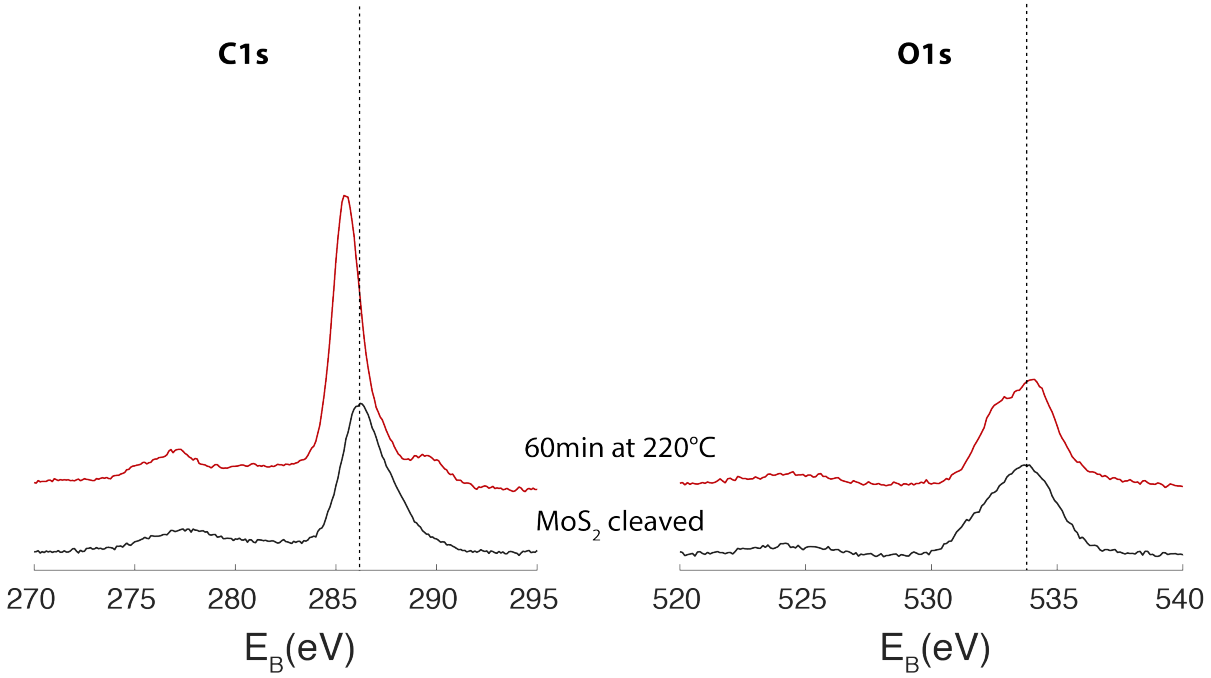

Figure 29: High resolution XPS spectra of the C1s and O1s line before and after evaporation of bixin.

Since the PES signal scales with the amount of atoms in the sample that it stems from, the ratio between the C1s and O1s intensities normalised by the corresponding photoionisation cross-sections reflects the ratio of carbon and oxygen atoms in the film. For determining this ratio the intensities were calculated by integrating the area under the peaks. The photoionisation cross-sections were taken from reference [67]. The results for each film are listed in Tab. 4. Comparing these ratios to the theoretically expected ones is a measure of determining the impact of the organic contamination on the substrate on the measured signal. It can be seen that the carbon-oxygen ratio of the thick curcumin film (60 min at 220°C) of 3.8 is closest to the expected ratio of 3.5 (21 carbon to 6 oxygen atoms). In the cases of the other curcumin films, the relative amount of oxygen is too small. In the case of bixin, the expected ratio is 6.25 (25 carbon to 4 oxygen atoms). The ratio of 5.7 found from the spectra therefore indicates a small excess of oxygen. The disagreement between the relative signal intensities and the expected ones can in both the case of bixin and curcumin be ascribed to contributions from substrate contaminants. This result underlines that the curcumin sample evaporated for 60 min at 220°C is the only sample that is thick enough to be studied independently of substrate contributions by PES. It also further supports the finding of the UV-Vis measurement that the curcumin molecule does not decompose during evaporation (see section 4.1).

Table 4: Overview of the intensity ratios between the C1s and the O1s lines normalised by photoionisation cross-section obtained on the evaporated curcumin and bixin films.

Sample	Normalised C1s/O1s intensity ratio
Curcumin	
15min @ 170°C	6.2
135min @ 170°C	5.5
60min @ 220°C	3.8
Bixin	
60min @ 220°C	5.7

Solution casting

The high resolution spectra of the C1s and O1s peaks measured on the solution-cast films were generally noisier than the ones measured on the evaporated films (see Fig. 30 compared to Fig. 28 and 29). Possible explanations for this could be that the evaporated films are more ordered and/or more homogeneously deposited onto the substrate. Bixin was found to not perfectly dissolve in ethanol even after a long time in the ultrasonic bath, and to precipitate quickly as soon as it was left unstirred. This likely lead to a very nonuniform film. Furthermore the dye-solvent ratio was much lower for bixin than for curcumin due to lower availability.
The peaks also showed a broader shape than those measured on the evaporated samples (more closely discussed in section 4.2.2) which lead to the suspicion that the ethanol had not fully evaporated and was contributing to the measured signals. To check for this, the samples were subjected to a heat treatment that would allow for evaporation of the remaining ethanol. Fig. 30 shows the C1s and O1s peaks at every step of the treatment for the curcumin and the bixin sample. The grey curves show a reference spectrum from a sample prepared only with pure ethanol and no dye. The curve labels indicate the annealing time of each consecutive heating step and the current applied to the sample holder. Since the temperature characteristics of the holder are not exactly known, the current was slowly increased throughout the heat treatment, while the chamber pressure was monitored. The increase in pressure indicated that material was being evaporated from the sample during annealing.

When comparing the pure ethanol spectrum to that measured on bare molybdenum disulfide (see Fig. 28 and 29), it can be seen that the main peaks are in the same position and the ethanol spectrum has small additional peaks. These could be attributed to the chemical shift of the C-O bond, while the rest of the spectrum stems from the same organic contamination as measured on the bare substrate. This is an indicator that the spectrum is dominated by the substrate contaminants.
Looking at curcumin (Fig. 30a), no significant changes in peak position, shape or intensity can be observed as the sample is annealed. The C1s peak lies at a slightly lower binding energy than that measured on pure ethanol; the O1s peak however is rather similar to that on pure ethanol. There is a slight increase in the intensity of the shoulder on the low energy binding side at roughly the position where the ethanol spectrum has a peak. After the final heat treatment of 240 min this effect however is undone again. The bixin spectrum differs more visibly from that measured on pure ethanol, especially the O1s

peak. Most notably, it has a peak near 530 eV (that appears to become more pronounced upon thermal annealing), which was not observed on the evaporated sample (see Fig. 29). The main peak remains around 533.5 eV, like that of the pure ethanol sample.
Based on the comparison between the pure ethanol and the bare substrate discussed above, the spectra of the solution-cast dyes are arguably more affected by the contribution from the substrate contaminants than the ethanol. What further supports this interpretation is the fact that the spectra change very little upon heating, i.e. the evaporation of possible ethanol remnants does not affect them. The reason for the contribution from substrate contaminants could be a consequence of the films being very thin. In this case, a different solvent would possibly yield different results, especially if it allowed for deposition of more uniform and thicker films. Another possible explanation is that contaminants from the substrate mix with the solution before the solvent is dried off, such that they are spread throughout the whole thickness of the film.

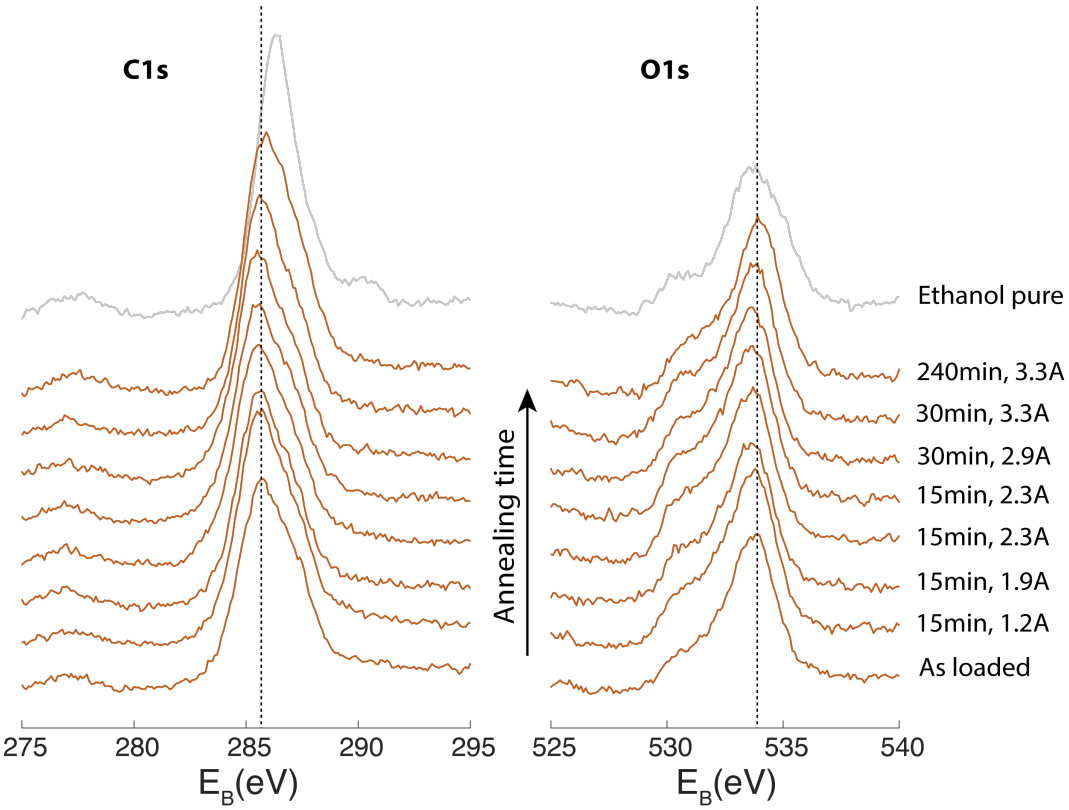

(a) Curcumin

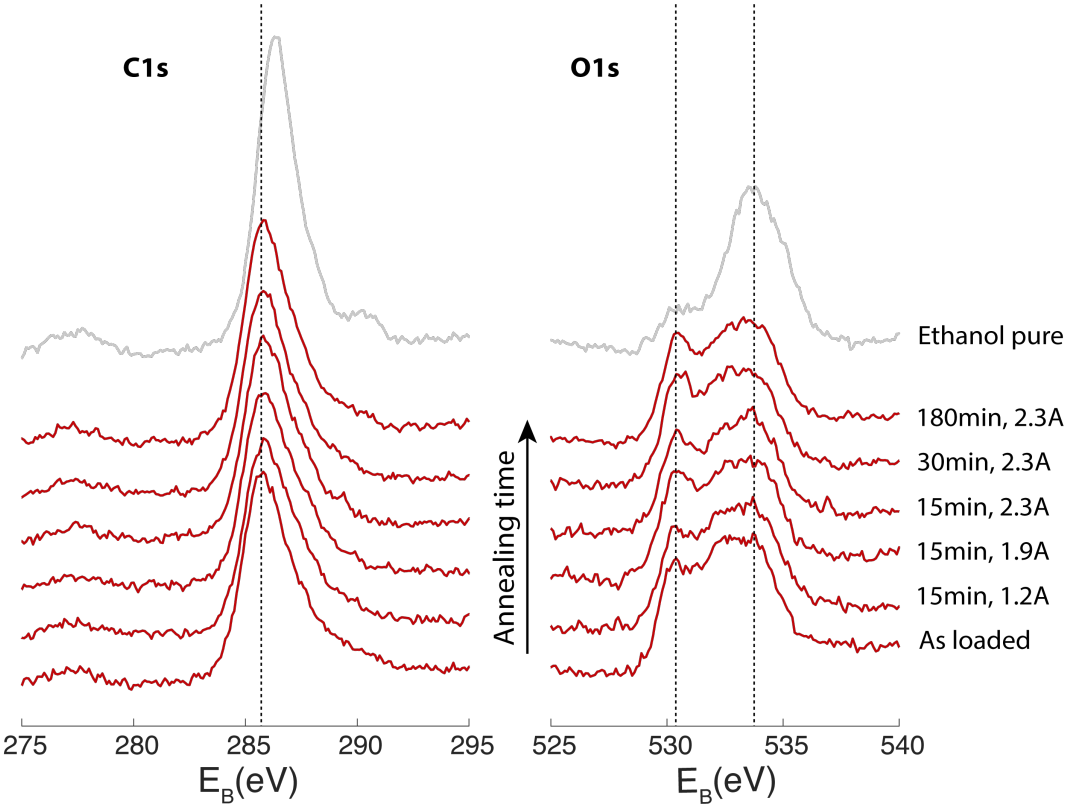

(b) Bixin

Figure 30: High resolution XPS spectra of the C1s and O1s line measured on solution-cast samples before annealing and after each annealing step. The grey line shows spectra measured on a pure ethanol sample.

4.2.2 Core levels

High resolution XPS spectra of the C1s and O1s state were recorded for a more careful investigation of the chemical composition of the films. Fig. 31 shows the measured and fitted C1s line of curcumin measured on an evaporated film (Fig. 31a) and a solution-cast film (Fig. 31b). The fitted Shirley background has been subtracted from the curves. Under each graph the residue curve is shown, which is calculated as the difference between the measured data and the fit. For better comparability, it is normalised to the maximum intensity of the corresponding spectrum.

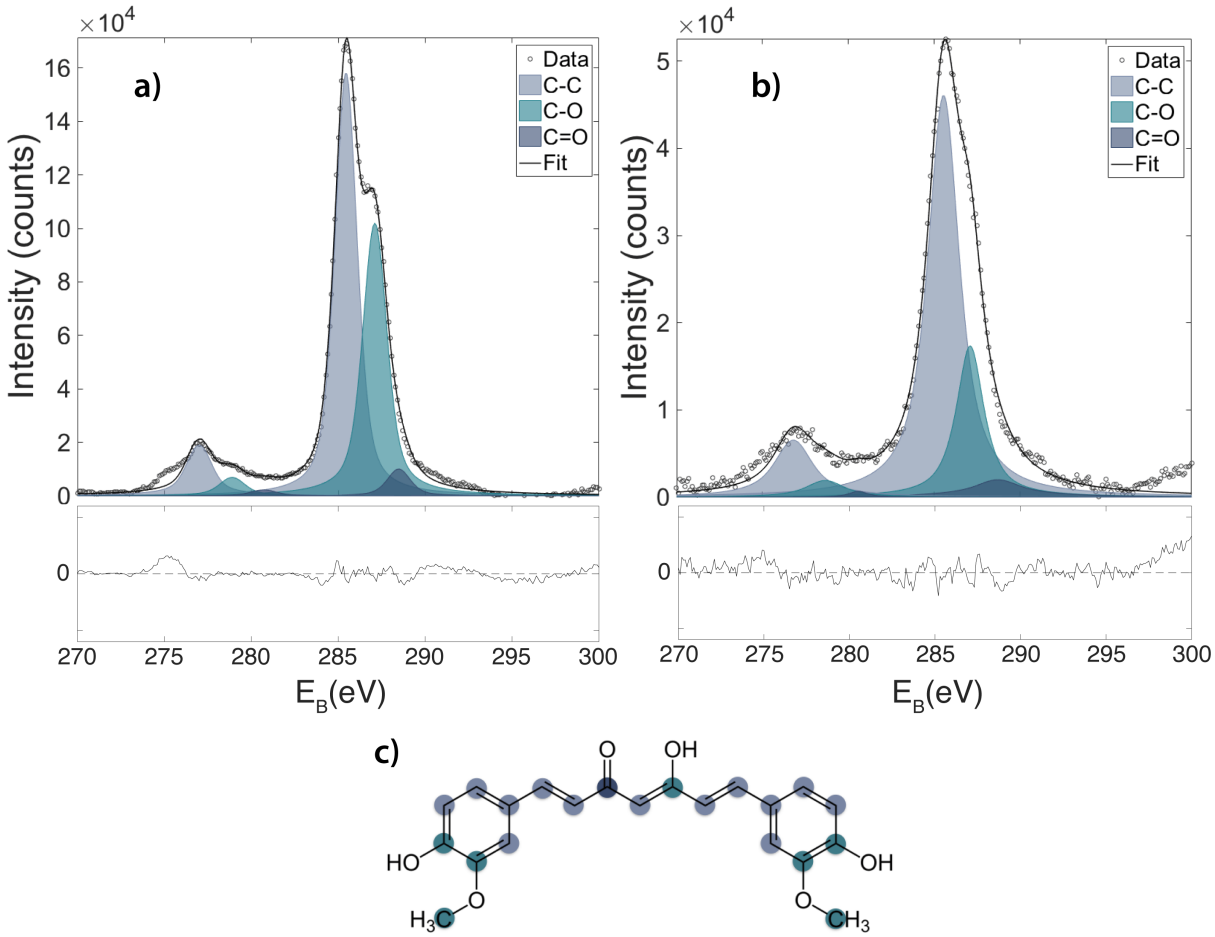

Figure 31: Fitted C1s line of curcumin measured by XPS on **a)** an evaporated film and **b)** a solution-cast film. The individual components of the fit represent the different types of carbon bonds occurring in curcumin, which are illustrated in **c)**.

The C1s main peak is located at 285.5 eV and a satellite peak arising from the $K_{\alpha 3}$ line of the magnesium anode of the X-ray source can be seen at an energy shift of -8.4 eV. The measured data is fitted with three components corresponding to the C–C bonds, the C–O bonds and the C=O bond, as illustrated in Fig. 31c. This is a simplification, as the C–C and C–O bonds in curcumin are not all the same; the energy resolution of the spectrum however is quite limited by the instrumentation. A more detailed analysis would require a synchrotron source. The largest considered component is therefore ascribed to the 13 C–C bonds of carbon bound to either two or three other carbon atoms. The second largest component are the 7 C–O bonds, which are both carbon atoms bound to two other carbon

atoms and one oxygen atom, as well as carbon atoms bound only to one oxygen atom. As oxygen has a higher electronegativity than carbon, this component is shifted towards higher binding energy. The C=O bond is shifted even further, as a result of the double bond. Curcumin possesses only one such bond, which is why this component is the weakest.

In Fig. 32, the C1s spectra measured on bixin are shown. Like in the case of curcumin, three components were considered here. In bixin, the C–C component stemming from 22 carbon atoms is even more dominant. It is followed by the C=O and the O–C=O carbons which were fitted as only one component, and finally the single C–O bond of the molecule. For bixin, the agreement between the measured data and the fit is much lower than for curcumin. This can be a result of higher contribution from the substrate contaminants due to the lower film thickness and uniformity discussed before. In the case of the evaporated sample, the degradation of the molecule discussed in section 4.1 certainly also plays a role.

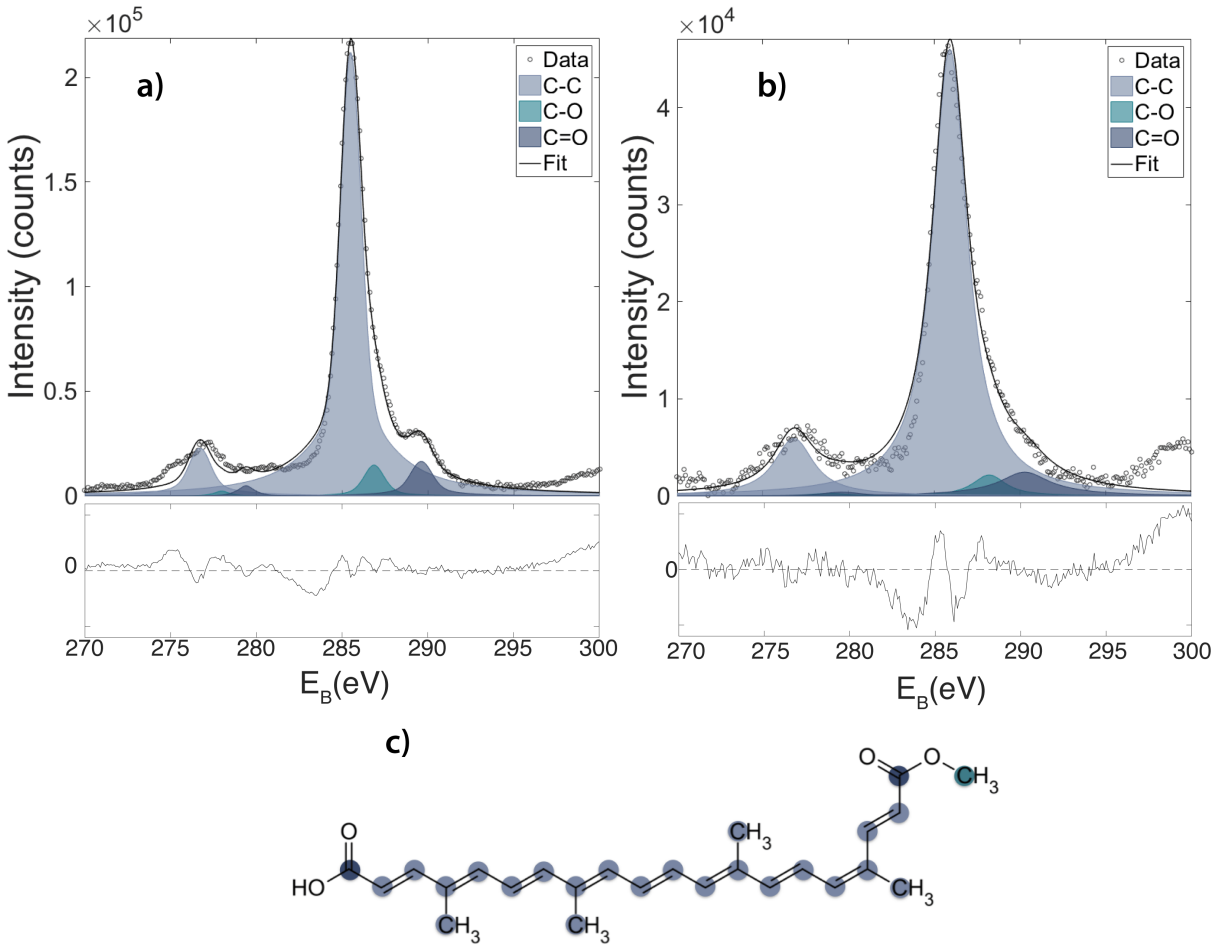

Figure 32: Fitted C1s line of bixin measured by XPS on **a)** an evaporated film and **b)** a solution-cast film. The individual components of the fit represent the different types of carbon bonds occurring in bixin, which are illustrated in **c)**.

For both curcumin and bixin, it can be seen that the main peak of the evaporated sample is around 3-4 times as intense as that of the solution-cast sample. The spectra measured on the solution-cast films are also much noisier, as is reflected in the residue curves. Furthermore, the spectra of the evaporated films allow for a distinction of two different

components by eye, while the solution-cast spectra in both cases only show one broad peak. This was initially assumed to be a result of contributions from ethanol still present on the sample, which however seems unlikely given that no change in the peak shape was observed upon annealing (see section 4.2.1). Substrate contaminant contributions therefore appear to be a more reasonable explanation. An alternative interpretation could be that the evaporated films have a higher degree of order, which can give rise to sharper peaks in XPS spectra. This difference between the two deposition methods is also reflected in the broadening of the fitted peaks. The Lorentzian widths of the fitted components in the spectra of the solution-cast samples are much larger than those of the evaporated samples. In both cases, however, the Lorentzian widths are too large to correspond to the broadening caused by the X-ray source and the hole-lifetimes, and are therefore assumed to be increased by the simplified consideration of only three components.
In the top part of Tab. 5 the binding energies of each fitted component are listed alongside values found in literature [68] for the corresponding bond. The difference from the literature values is indicated. For the curcumin samples it is found that the fitted components are shifted in binding energy from the literature values, but the relative chemical shift is similar. The peak positions on the bixin sample are very far off as a result of the low quality of the data and the simplified fit.
The area of each component's peak corresponds to the intensity of the signal caused by that bond. The ratio between the areas of the individual peaks should therefore reflect the number ratio between the bonding types occurring in the molecule. In the bottom part of Tab. 5 the component ratios of the fitted data are compared to the expected ratios. On all samples the ratios are found to deviate relatively strongly from the expected ones, which is not surprising given the data quality and the simplifications made in the fit.

Table 5: Overview of the binding energies and intensity ratios of the fitted components in the C1s peak on curcumin and bixin, alongside literature values from reference [68] and theoretical expectations (grey cells).

	Binding energy in eV									
	Curcumin					**Bixin**				
		Evap.	Diff.	Sol.	Diff.		Evap.	Diff.	Sol.	Diff.
C–C	284.8	285.4	0.6	285.6	0.8	284.8	285.5	0.7	285.9	1.1
C–O	286.3	287.1	0.8	287.1	0.8	286.3	286.9	0.6	288.2	1.9
C=O	287.8	288.5	0.7	288.7	0.9	287.8	289.6	1.8	290.3	2.5

	Component intensity ratios					
	Curcumin			**Bixin**		
		Evap.	Sol.		Evap.	Sol.
1 : 2	1.86	1.4	3.1	22	20.6	22.9
1 : 3	13	15.1	13.3	11	15.0	12.1
2 : 3	7	10.8	4.3	0.5	0.7	0.7

4.2.3 Valence band

The valence band spectra measured by UPS on evaporated and solution-cast curcumin are shown in Fig. 33. In order to eliminate contributions from the substrate, the thickest evaporated sample (60 min at 220°C) was used for the UPS measurements. The differently coloured curves represent different positions on the sample. On the evaporated sample (Fig. 33a), before the high resolution measurement at each position a quick scan was performed, shown as a dashed line. The purpose of this was to check whether the exposure to UV light leads to changes in the spectrum. It can be seen that the intensity of the quick scans is higher than that of the corresponding long scans below -2 eV, but this difference is on the same order as the fluctuations between the individual positions. These fluctuations are stronger on the solution-cast sample (Fig. 33b) and continue above -2 eV, further supporting the assumption that the solution-cast film is less uniform.

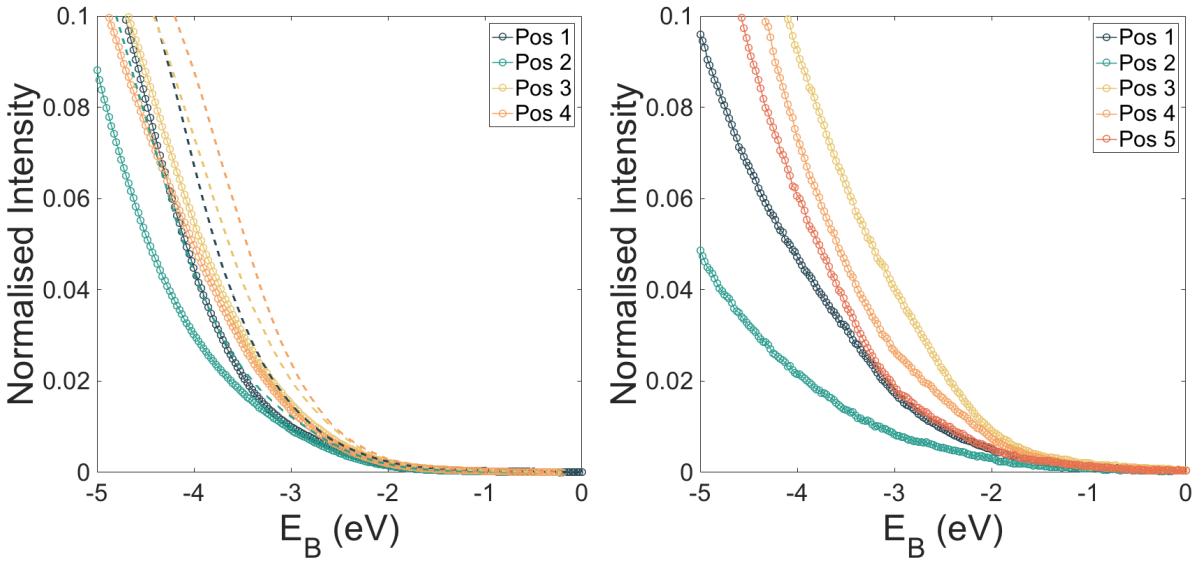

(a) Evaporated (b) Solution-cast

Figure 33: UPS measurement on **(a)** evaporated and **(b)** solution-cast curcumin films on molybdenum disulfide substrate. Different colours represent different positions on the sample; the dashed lines in **(a)** show quick scans taken before the high resolution measurements.

The corresponding results for bixin are shown in Fig. 34. In the case of the evaporated sample (Fig. 34a), one position was measured at the beginning of the series and again in the end after measuring all the other positions. There is quite a large discrepancy between the signal strength of the two measurements, however the peak positions remain the same. On both samples it is generally found that the signal strength varies quite strongly between the individual positions, but the peak positions appear to be similar. The evaporated sample shows peaks at around -3.6 eV and -2.4 eV, which are not observed in the solution cast sample, and the signal drops to zero at ca. -1.5 eV. Given the very low thickness of the film, it is likely that the features observed on the evaporated sample stem from the molybdenum disulfide substrate. The signal of the solution-cast sample, on the other hand, may have a contribution from the solvent. In order to test for that, the sample was annealed for 30 min and the measurement was repeated. The result of this can be seen in Fig. 35a. The curves show no peaks anymore, but drop to zero around a similar value as before the anneal.

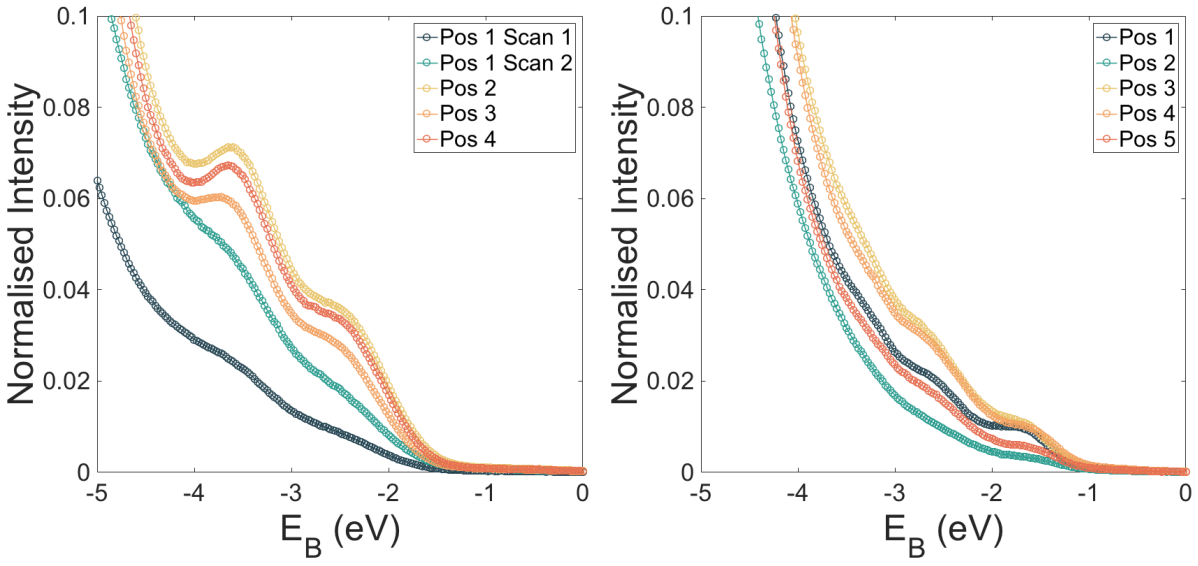

(a) Evaporated (b) Solution-cast

Figure 34: UPS measurement of **(a)** evaporated and **(b)** solution-cast bixin films on molybdenum disulfide substrate. Different colours represent different positions on the sample.

Additionally, a sample of only ethanol not containing any bixin was measured in order to separate the signal from that of the bixin. The corresponding result is shown in Fig. 35b. The curves at position 1 and, to a lesser degree, at position 2 show a peak at -2.8 eV, a feature that appears to be reflected in the curves of the solution-cast sample (Fig. 34b). However, the latter possesses another peak at ca. -1.6 eV, which is not observed on the ethanol spectrum. Since this does not originate from molybdenum disulfide either, it is likely to be a feature of bixin.

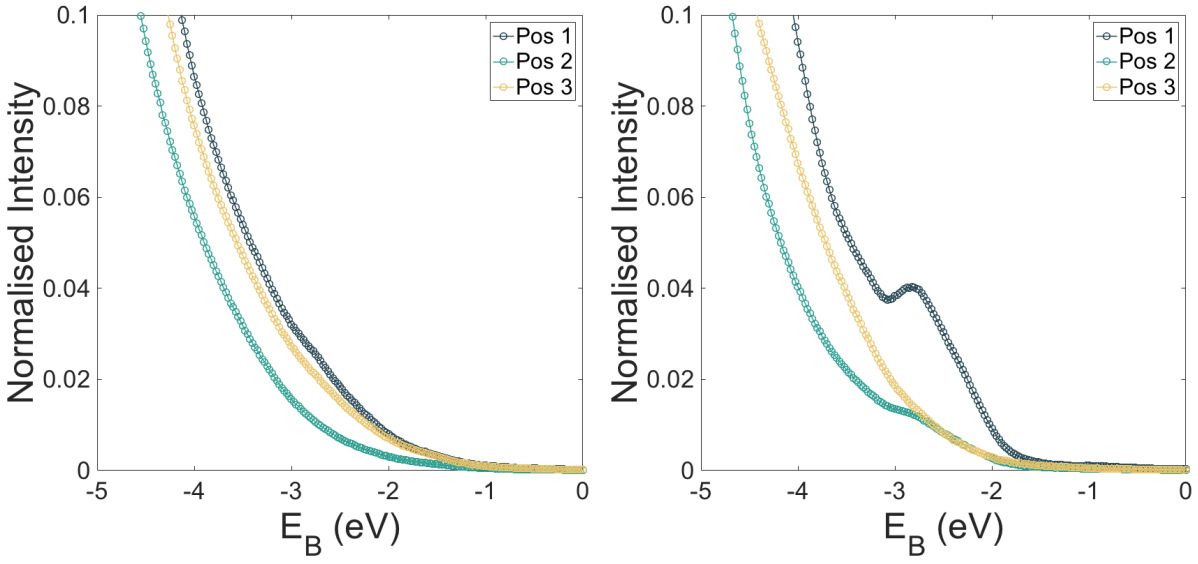

(a) Solution-cast after annealing (b) Solvent only

Figure 35: UPS measurement on **(a)** the solution-cast bixin sample after annealing and **(b)** a pure ethanol sample.

4.2.4 Band gap

The band gaps of the molecules were determined from combined UPS and IPES spectra. As a result of the considerations made in section 4.2.3, the calculation of the band gap was based on the evaporated curcumin film spectra, while for bixin those of the solution-cast film were taken. The graphs in Fig. 36 show the intensity normalised UPS spectra, which were averaged over all positions, together with the IPES spectra. The latter were only measured on evaporated films. It should be noted that the signal obtained in the IPES measurement was significantly lower than that in the UPS measurement.

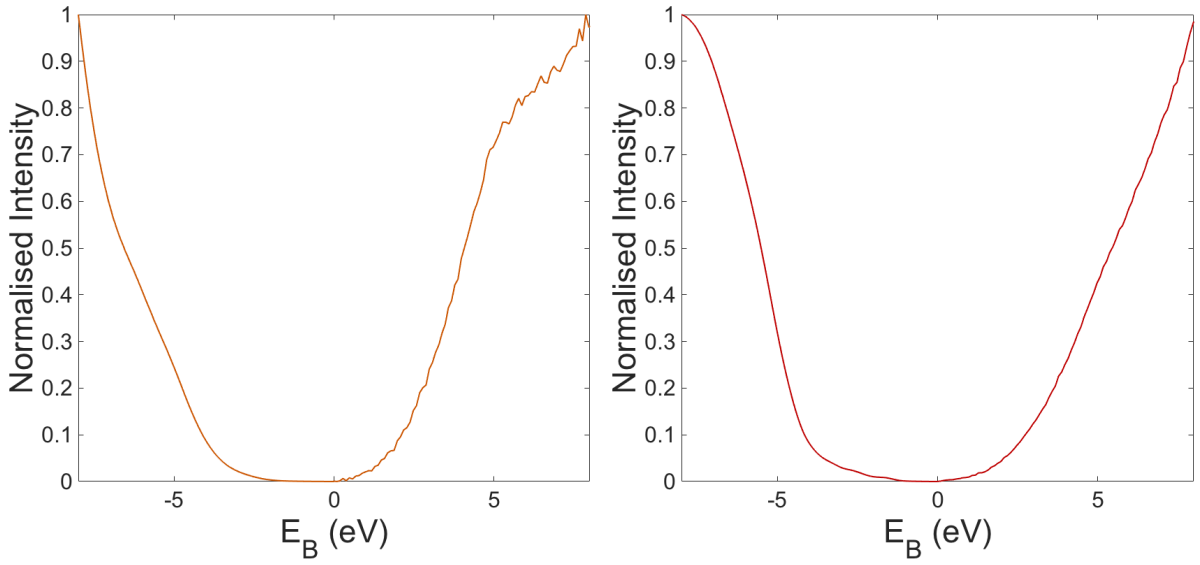

(a) Curcumin (b) Bixin

Figure 36: Combined UPS and IPES spectra for curcumin and bixin.

In order to determine the valence and conduction band edges, linear fits were applied to the UPS and IPES data, respectively, and their intersection with the x-axis recorded. The tail of the IPES data is a result of the gradual onset of photoionisation in the sodium chloride coated photocathode in the detector (see section 3.3.4). It is therefore not considered to be actual signal from the sample. This is why the linear fit is applied to the straight section of the curve as shown in Fig. 37b. The intersection points of the linear fits with the x-axis mark the valence and the conduction band edge. The band gap was then determined as the energy difference between the band edges. The results of this are listed in Tab. 6, together with the values obtained from the UV-Vis absorption spectra for comparison.

It is found that there is rather good agreement between the experimentally determined band gap sizes of curcumin. The values found for bixin are in both cases larger than for curcumin, which is contrary to the expectation (based on the colours of the dyes), but likely explainable by the damaging of the molecule upon thermal evaporation (as discussed in section 4.1). This could be the reason for the high conduction band edge found in the IPES measurement on evaporated bixin, which is the main cause for the difference in band gaps between the two molecules (see Fig. 37). In addition to that, neither the IPES nor the UPS signal obtained on bixin is free from contributions from substrate contaminants, which has been discussed in the previous sections. This is expected to introduce high

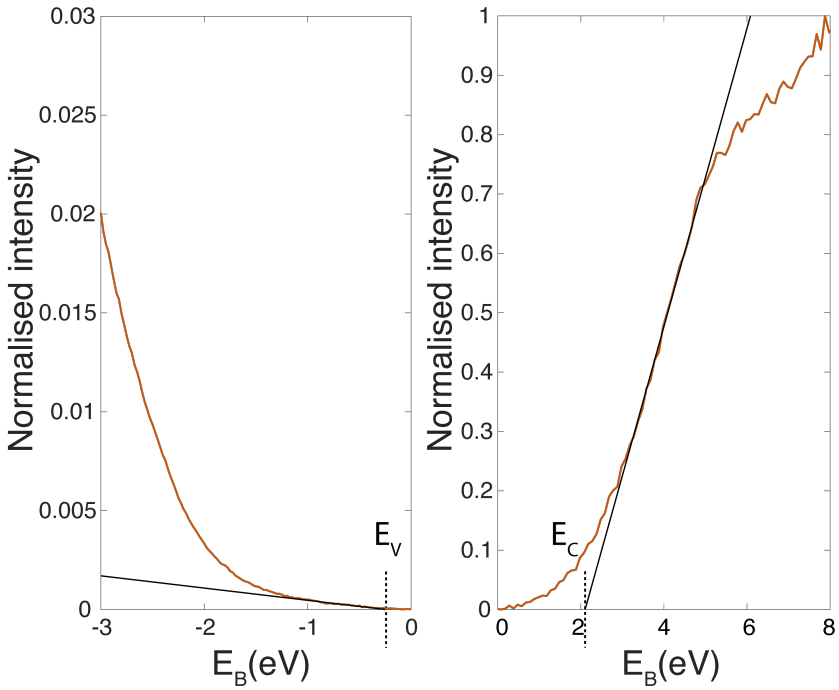

(a) Curcumin

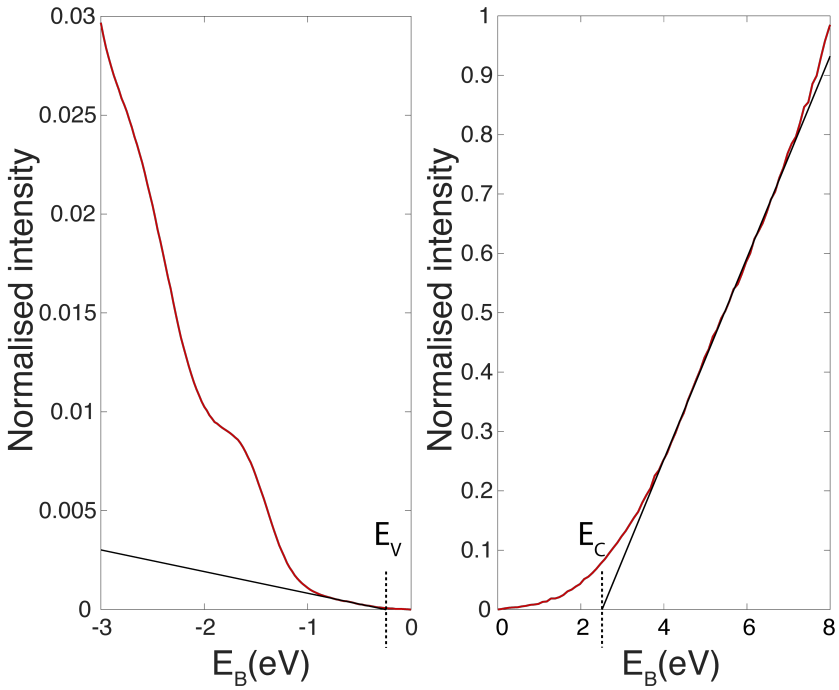

(b) Bixin

Figure 37: UPS (left) and IPES (right) spectra of curcumin and bixin with linear regressions to determine the band edges. The dotted lines mark the obtained valence and conduction band edges.

uncertainties in the determination of the band edges and thus the band gap. The obtained value for the band gap of curcumin from UPS and IPES measurements taken on a thick evaporated sample is therefore considered more reliable.
In both curcumin and bixin the valence band edge is found to be much closer to the Fermi level than the conduction band edge. This means that the materials are p-type

in character, i.e. that they are hole-conducting materials, as is the case for most organic semiconductors [69]. p or n-type character is one of the basic requirements for an organic solar cell material in order to allow for a junction to form [70].

Table 6: Comparison of the band gaps of curcumin and bixin obtained from absorption spectroscopy and photoemission spectroscopy.

	Band gap [eV]	
	Curcumin	Bixin
Obtained from UV-Vis	2.3	2.5
Obtained from PES	2.4	2.8

4.2.5 Beam damage testing

The exposure to energetic electromagnetic radiation as well as electron bombardment can cause notable damage to sensitive samples (which is often the case with organic materials) and thereby alter the results of the measurement. For precaution, the duration of the beam exposure was minimised in all PES measurements.
In an attempt to monitor whether damage was caused, the IPES measurements were taken as a sequence of many short scans to be averaged later. Fig. 38a shows such a sequence of 5 individual scans measured consecutively at the same position on the evaporated curcumin sample. The signal becomes increasingly noisy towards higher binding energies, but no systematic development can be observed between the scans. In Fig. 38b measurements from different positions on the curcumin sample are shown. After all positions were measured, the measurement on position 1 was repeated. The difference between those two measurements is smaller than the fluctuations seen between different position and can possibly be explained by a slight discrepancy between the actual sample positions.

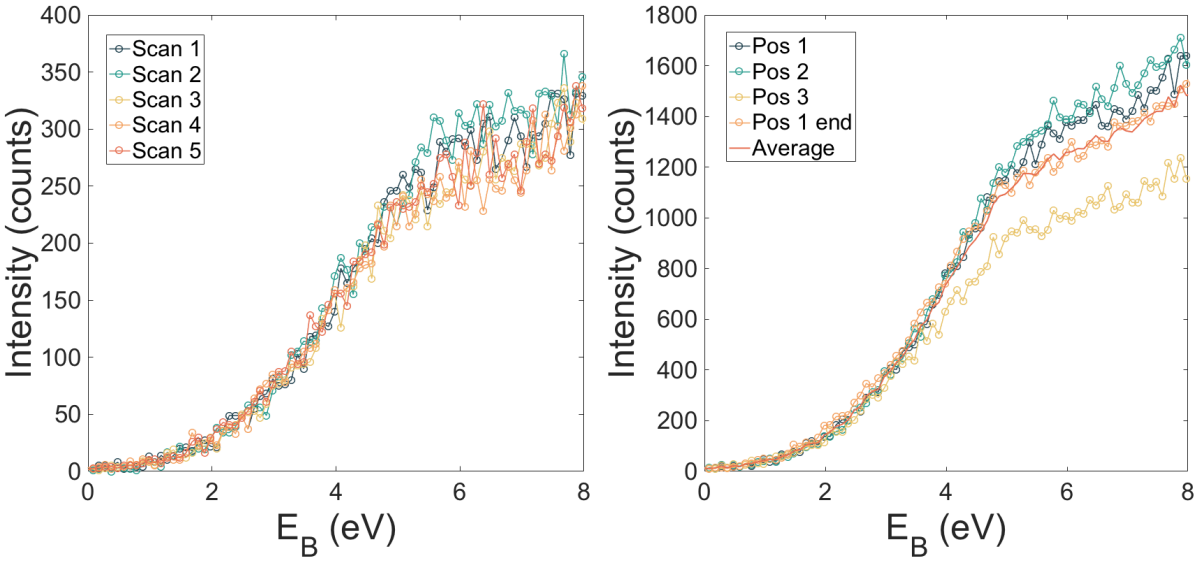

(a) (b)

Figure 38: Individual IPES spectra measured on the evaporated curcumin sample. **(a)** A series of scans measured at the same position. **(b)** A series of measurements at different positions on the sample.

The red curve is the average of the spectra, which was used for the determination of the conduction band edge. On the bixin sample the same measuring procedure was applied and showed the same result. The electron beam therefore apparently causes no damage that would lead to an explicit change in the unoccupied energy states.
Another check for beam damage on the evaporated curcumin film was done by comparing high resolution XPS spectra of the C1s and the O1s line after IPES and UPS measurements to the initial measurement. These are shown in Fig. 39. The spectra are identical apart from a minimal shift of the peak position towards lower binding energies in both the C1s and the O1s line. This indicates that the overall composition of the film was not significantly affected by the UPS and IPES measurements. Since the XPS signal stems from a larger area than that of the other PES techniques, this does, however, not entirely eliminate the possibility that damage was done very locally.

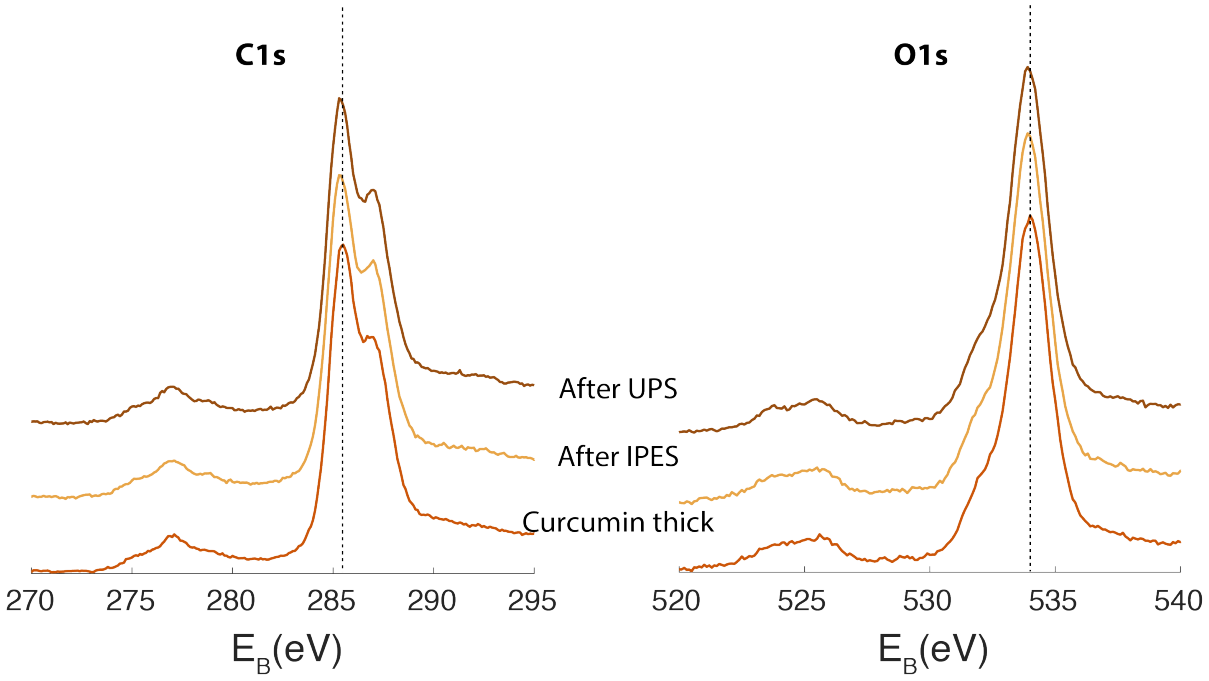

Figure 39: XPS spectra of the C1s and the O1s line measured on the thick curcumin sample before and after UPS and IPES measurement to check for beam damage.

4.3 Crystal structure

Powder diffraction was successfully performed on both curcumin and bixin. The diffraction pattern measured on curcumin powder is shown in Fig. 40 (orange curve). It is presented together with a simulated pattern resulting from unit cell refinement using the Pawley method [71] performed with the software *Topas* (black curve). The main peaks are indexed with the corresponding reflection plane. It can be seen that the sample exhibits very sharp and intense peaks, which is generally an indicator for a high degree of crystallinity. As the starting point for the refinement, experimentally determined lattice parameters from reference [72], obtained in a similar experiment, were used. Comparing the two patterns one can see that the positions of the peaks match very well, while the peak intensities are quite off. There is a large discrepancy especially between the (202), the (020) and the (010) reflections. There is a number of possible sources for these discrepancies, the most important ones being a difference between the real atom positions and the simulated ones, as well as the occupancy of atomic sites. Furthermore, the crystallites in the powder could have a preferred orientation that is not accounted for in the simulation. In order to extract this information, additional refinements would have to be performed in the next step.

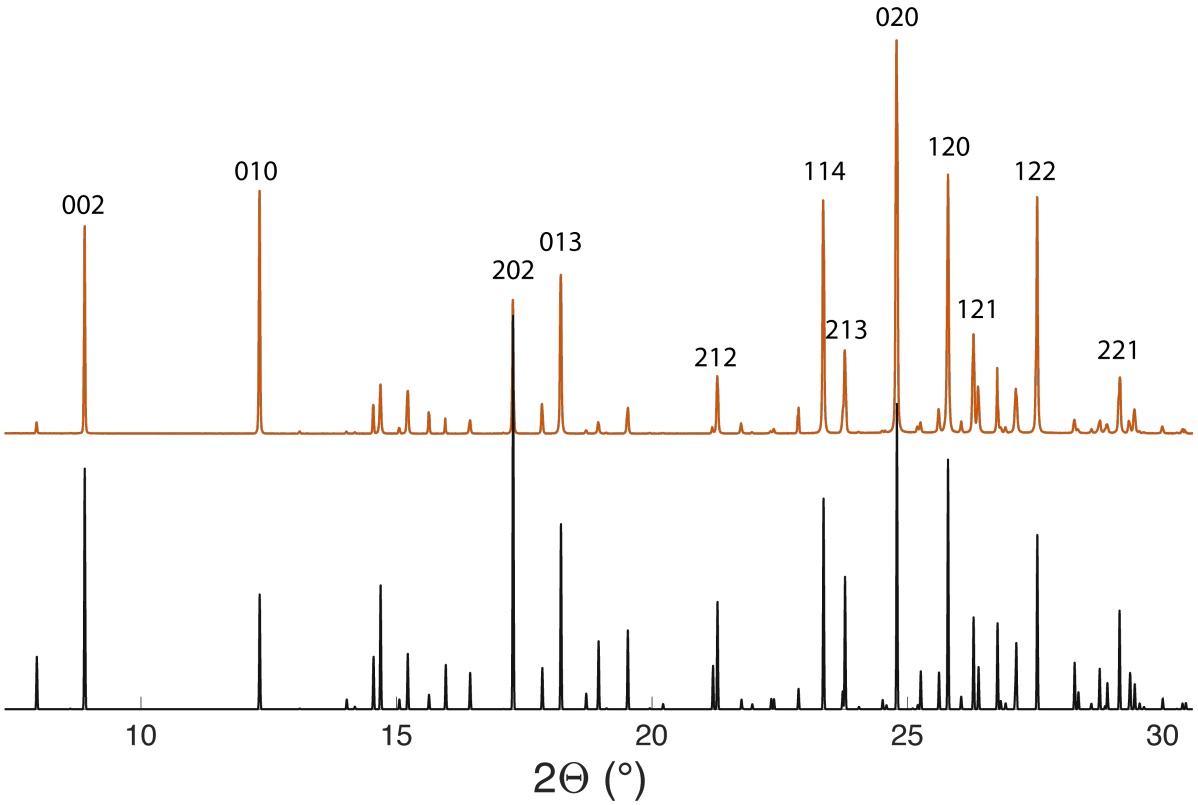

Figure 40: Measured curcumin powder diffraction pattern (orange) and simulated pattern after Pawley refinement of the unit cell (black). The refinement was performed with *Topas* and the simulated diffraction pattern created by *CrystalDiffract*.

The refined lattice parameters were found to be $a = 12.7419(3)$ Å, $b = 7.2202(3)$ Å, $c = 20.0530(9)$ Å and $\beta = 94.9801(1)°$. These values are very close to the parameters reported in [72].

A model of the obtained curcumin unit cell created with CrystalMaker can be seen in Fig. 41. It has a volume of 1837.914 $Å^3$ with 188 sites per unit cell. The crystal structure of curcumin is monoclinic and it belongs to the space group 2p/n.

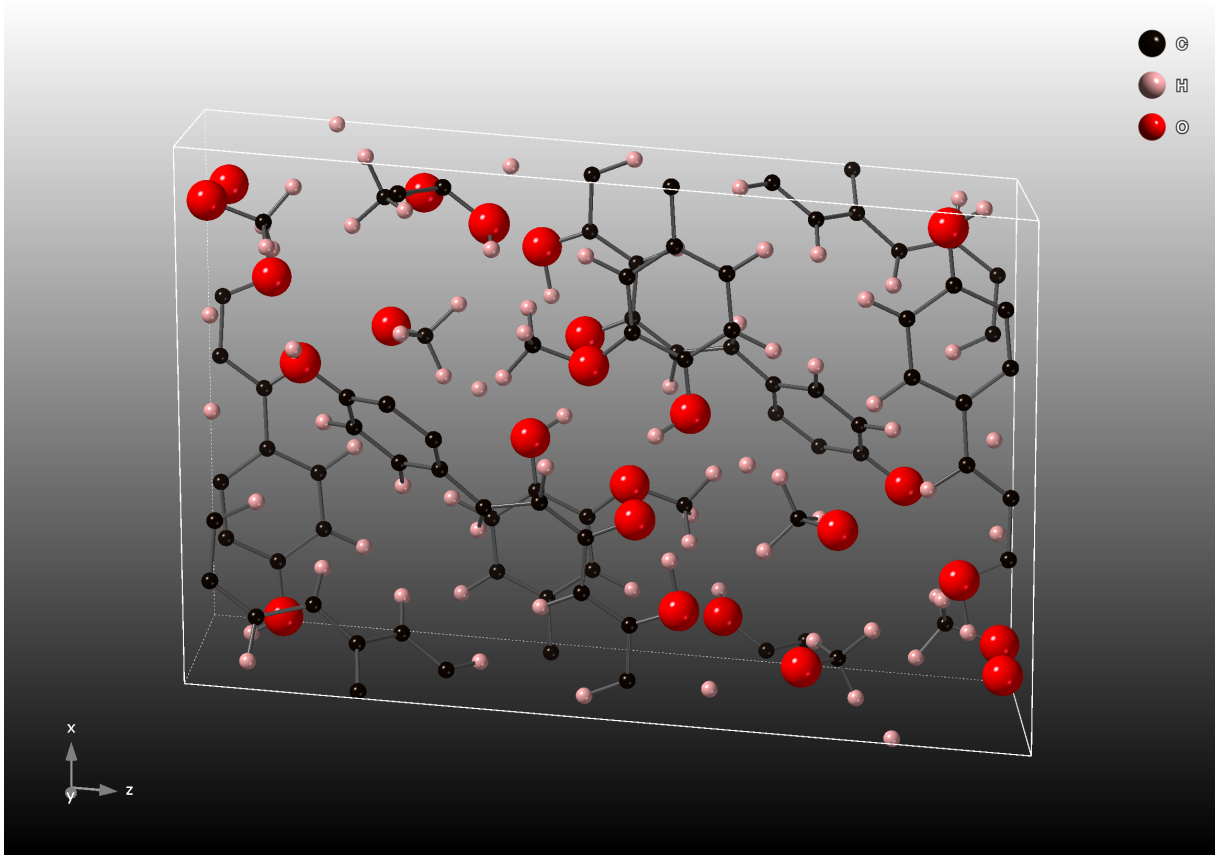

Figure 41: Model of the refined unit cell of curcumin created with *CrystalMaker*.

Another diffraction pattern was measured after annealing the curcumin powder at 200°C, whereby it melted and recrystallised. The result of that measurement is seen in Fig. 42. The simulated pattern from Fig. 40 is shown again for comparison. It can be seen that the peaks have shifted, some having moved in one direction and others in the other. The relative peak intensities have also changed. The (002) reflection is now the most intense, followed by the (202) reflection.
The signal strength of the annealed curcumin sample was found to be much lower than that of the unannealed powder. A possible interpretation of this is that the crystallites in the sample are not randomly oriented anymore and the crystal orientation with respect to the beam is such that the main diffraction peaks cannot be observed in the range scanned by the detector. Testing this hypothesis would have required being able to rotate the sample, which was not possible with the given setup.

The background-subtracted diffraction pattern measured on bixin powder can be seen in Fig. 43. Very little has been published about bixin, and, to the author's knowledge, no synchrotron XRD has ever been performed on bixin. Since the crystal structure and space group are unknown, no refinement was performed at this point. Theoretical density functional theory (DFT) calculations are expected to provide a starting point for a thorough analysis of the measured spectrum. Compared to the curcumin powder sample, the signal

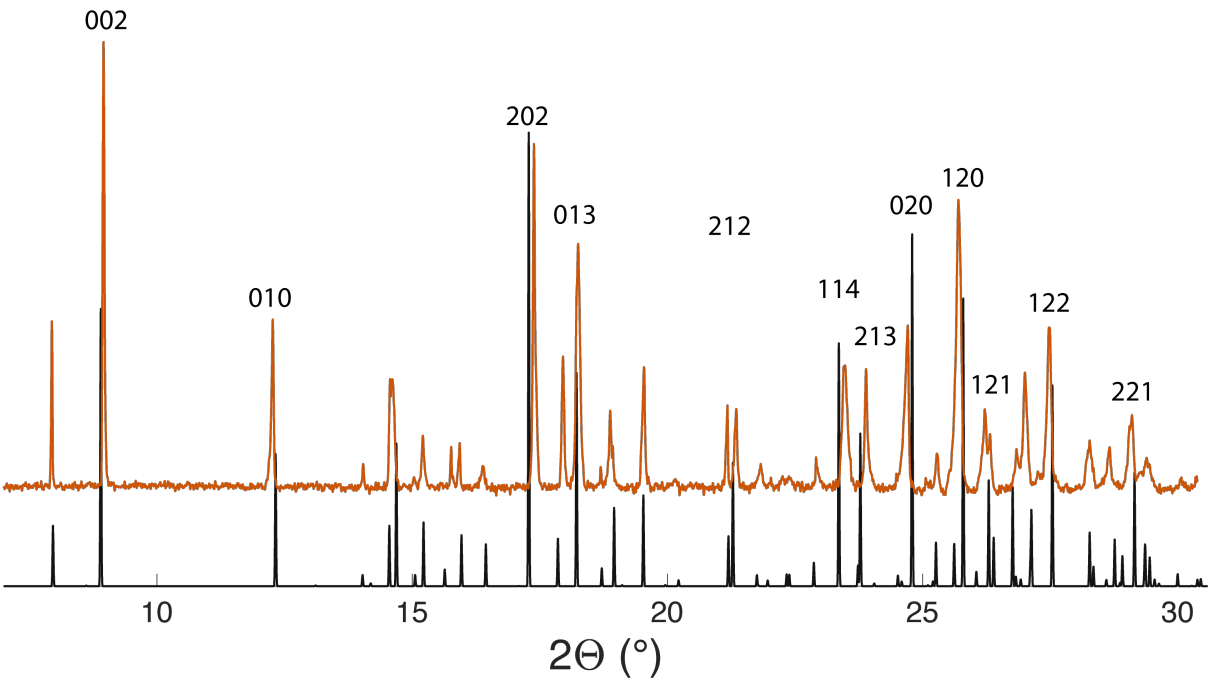

Figure 42: Measured diffraction pattern of curcumin powder after annealing at 200°C (yellow) and simulated pattern from Fig. 40 (black).

intensity measured on bixin powder was much weaker. This is an indicator that the degree of crystallinity of the molecule in powder form is lower.

Unfortunately, none of the evaporated films showed any signal in the XRD measurement. While the thickness of those films is not exactly known, it is likely <1 µm (based on estimates of the deposition rate from thickness measurements, see section 4.2.1). For an organic material consisting of only carbon and oxygen, such a thin film apparently does not have enough scattering power to give a measurable signal. The given setup of the beamline did not allow for measuring the samples at grazing incidence, which increases the signal strength by increasing the irradiated volume of the sample [73]. This is something that could be considered in future investigations. Diffraction patterns measured on solution-cast films on mylar substrate showed very little (curcumin) or no (bixin) signal, which is most likely also a result of the films being very thin. Additionally, measurements on pure mylar substrate showed a broad diffraction peak in the considered range (around 16.3°), which shows that it was not the most suitable substrate in this experiment. Measurements on the pure aluminium foil on the other hand revealed no diffraction peaks at all, suggesting this to be the substrate of choice in future investigations.

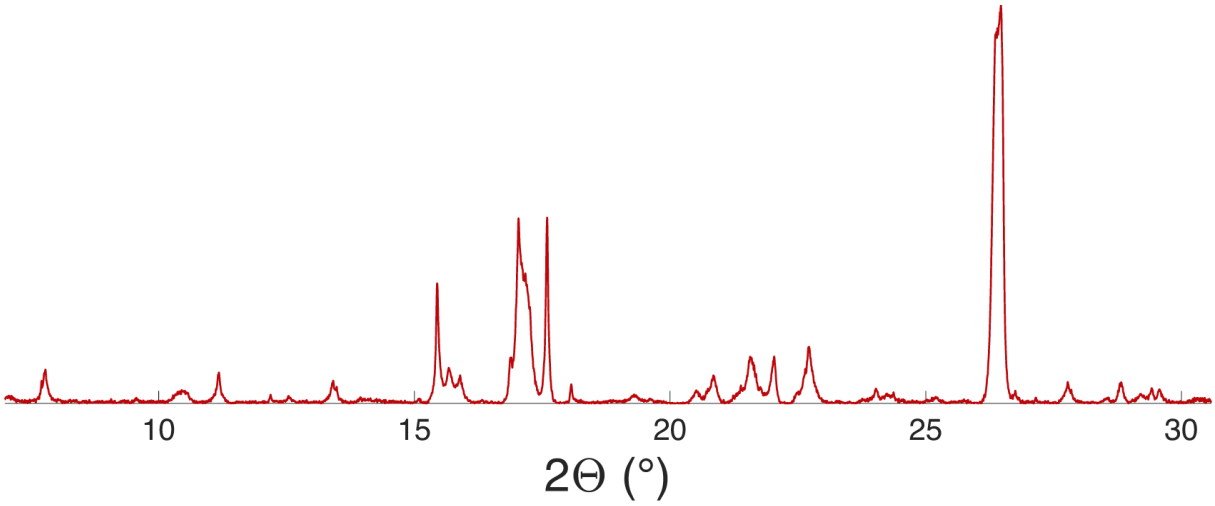

Figure 43: Measured diffraction pattern of bixin powder.

5 Conclusion and Outlook

The aim of the presented work was to study semiconducting natural dyes to form a basis on which their applicability in organic solar cells can be assessed. For this purpose, films were prepared using thermal evaporation and solution processing. The characterisation of the films included the investigation of optical absorption properties, as well as electronic and crystalline structure.

In the preparation of the films it became clear that curcumin is easier to handle than bixin for several reasons. For the first part, because there is a large discrepancy in prices for the two molecules in high purity form, which is why curcumin was available in greater quantities. This enabled the growth of films by thermal evaporation, that resulted thick enough to eliminate contributions from organic substrate contaminants in PES measurements. Curcumin also displayed better solubility in ethanol, facilitating higher uniformity of films prepared by solution-casting. UV-Vis measurements on thermally evaporated films indicated that the curcumin molecule remained intact under the influence of heat. The absorption spectrum of evaporated bixin, on the other hand, was found to shift to shorter wavelengths, which was also visibly reflected in the film's yellow colour, indicating chemical degradation of the molecule. The difficulty to obtain a sufficiently thick bixin film complicated the interpretation of PES spectra, as substrate contributions had to be taken into account.

High resolution XPS spectra of the C1s line on evaporated samples showed chemical shifts resulting from different chemical environments of the carbon atoms. On solution-cast films, the shifts were less clearly resolved, possibly as a result of organic contamination or a less ordered film structure. Given the limited resolution of the spectra attainable with the used XPS system, the data was fitted with three components, merging together chemical bonds expected to cause similar shifts. For curcumin, relatively good agreement was found between the fit and the measured data, while for the bixin spectra no satisfactory fit could be made. This is probably a result of insufficient film thickness, as well as low uniformity in the case of the solution-cast sample. In the case of the evaporated bixin sample, the chemical degradation observed in the optical absorption spectrum likely renders the chosen fitting components inadequate.

From combined UPS and IPES measurements, the band gaps of the molecules were determined. For curcumin, the obtained value of 2.4 eV was in good agreement with that obtained from UV-Vis (2.3 eV). For bixin, PES and UV-Vis measurements resulted in band gap sizes of 2.5 eV, and 2.8 eV, respectively; the reason for the discrepancy likely being low data quality in both measurements as a result of the films being very thin. The position of the Fermi level with regards to the conduction and the valence band edges revealed that both molecules have p-type character.

In terms of stability under exposure to energetic electromagnetic radiation and electrons in the PES measurements, no strong indicators of damage were observed. Given the very short exposure times during the experiment, this does however not rule out that degradation can occur on longer time frames.

From XRD measurements on powder, a Pawley unit cell refinement of curcumin was performed, yielding the lattice parameters $a = 12.7419(3)$ Å, $b = 7.2202(3)$ Å, $c = 20.0530(9)$ Å and $\beta = 94.9801(1)^\circ$ Annealing of the curcumin sample was found to lead to peak shifts in the diffraction pattern and a lower signal intensity, which could be a consequence of a higher degree of crystalline order and a "wrong" orientation of the sample with respect to the beam. Powder diffraction was also successfully performed on bixin,

displaying lower crystalline order than curcumin. XRD measurements on solution-cast samples showed very weak signal and those on evaporated films proved completely unsuccessful, due to insufficient thickness of the films.

In summary, it has been found that curcumin is superior to bixin in terms of processability, stability and crystalline order (in powder form). These properties are favourable for an organic solar cell material, but further research, e.g. on the crystalline order of deposited films, is needed. Still, curcumin can be considered a promising candidate material. For bixin, on the other hand, the experimental results were in many cases limited by the low availability of the molecule, preventing the deposition of sufficiently thick films. Considering that solution-processing is generally cheaper and faster than thermal evaporation and therefore the deposition method of choice in commercially processed organic solar cells, the damaging of bixin upon evaporation does not necessarily obstruct its applicability in OPV.

For future studies it could be considered to synthesise bixin from annatto (as described in reference [74]), as the high price of high purity bixin represents an obstacle not only for investigation but also application. This would presumably allow for the formation of thicker films, enabling a more meaningful analysis. Similarly, having studied the properties of high purity curcumin, in a next step it could be interesting to look at less pure (and therefore cheaper) forms, such as turmeric powder commonly used in the kitchen.
Since for solar cell materials stability under UV light is of great importance, looking into the effect of longer UV exposure on the molecules is necessary.
As for the XRD results, additional refinement methods taking into account the relative peak intensities are expected to reveal more information on the atomic positions in the unit cell of curcumin, as well as preferred crystal orientations and changes in the crystalline structure upon annealing. The diffraction pattern measured on bixin will, in combination with computational DFT calculations, be used in the next step to determine the crystal structure of bixin. Additionally, repeating the measurement on thicker evaporated films would allow for checking the hypothesis that films deposited by thermal evaporation are more ordered. A grazing-incidence geometry of the XRD setup could furthermore be used to increase the signal strength on thin films.
Future work should also look closely into whether the suggested effect of reduced carrier trapping in diluted semiconductors [11] can be observed in blends of the studied dyes with polymeric host matrices, as this could be a very relevant manifest application.

References

[1] D. Kearns and M. Calvin. “Photovoltaic Effect and Photoconductivity in Laminated Organic Systems”. In: *The Journal of Chemical Physics* 29.4 (1958), pp. 950–951.

[2] D.L. Morel, E.L. Stogryn, A.K. Ghosh, T. Feng, P.E. Purwin, R.F. Shaw, C. Fishman, G.R. Bird, and A.P. Piechowski. “Organic photovoltaic cells. Correlations between cell performance and molecular structure”. In: *The Journal of Physical Chemistry* 88.5 (1984), pp. 923–933.

[3] C.W. Tang and A.C. Albrecht. “Photovoltaic effects of metal–chlorophyll-a–metal sandwich cells”. In: *The Journal of Chemical Physics* 62.6 (1975), pp. 2139–2149.

[4] S. Singh and B.B. Aggarwal. “Activation of Transcription Factor NF-κB Is Suppressed by Curcumin (Diferuloylmethane)”. In: *Journal of Biological Chemistry* 270.42 (1995), pp. 24995–25000.

[5] K. Priyadarsini. “The Chemistry of Curcumin: From Extraction to Therapeutic Agent”. In: *Molecules* 19.12 (2014), pp. 20091–20112.

[6] M.J. Scotter, L.A. Wilson, G.P. Appleton, and L. Castle. “Analysis of Annatto (Bixa orellana) Food Coloring Formulations. 2. Determination of Aromatic Hydrocarbon Thermal Degradation Products by Gas Chromatography”. In: *Journal of Agricultural and Food Chemistry* 48.2 (1999), pp. 484–488.

[7] D. Das and S. Chandra Bhattacharya. “Dyeing of wool and silk with Bixa orellana”. In: *Indian Journal of Fibre and Textile Research* 32.3 (2007), pp. 366–372.

[8] K.E. Jasim, S. Cassidy, F.Z. Henari, and A.A. Dakhel. “Curcumin Dye-Sensitized Solar Cell”. In: *Journal of Energy and Power Engineering* 11.6 (2017), pp. 1–9.

[9] A. Hiendro, F. Hadary, W. Rahmalia, and N. Wahyuni. “Enhanced performance of bixin sensitized TiO_2 solar cells with activated kaolinite”. In: *2012 International Conference on Enabling Science and Nanotechnology (ESciNano)*. IEEE, 2012, pp. 1–2.

[10] N.M. Gómez-Ortíz, I.A. Vázquez-Maldonado, A.R. Pérez-Espadas, G.J. Mena-Rejón, J.A. Azamar-Barrios, and G. Oskam. “Dye-sensitized solar cells with natural dyes extracted from achiote seeds”. In: *Solar Energy Materials and Solar Cells* 94.1 (2010), pp. 40–44.

[11] D. Abbaszadeh, A. Kunz, G.A.H. Wetzelaer, J.J. Michels, N.I. Crăciun, K. Koynov, I. Lieberwirth, and P.W.M. Blom. “Elimination of charge carrier trapping in diluted semiconductors”. In: *Nature Materials* 15.6 (2016), pp. 628–633.

[12] S. Zhang, L. Ye, H. Zhang, and J. Hou. “Green-solvent-processable organic solar cells”. In: *Materials Today* 19.9 (2016), pp. 533–543.

[13] W.C.H. Choy. *Organic solar cells: materials and device physics*. Green energy and technology. London: Springer, 2014.

[14] E.D. Głowacki, N.S. Sariciftci, and C.W. Tang. “Organic Solar Cells”. In: *Solar Energy*. New York: Springer, 2013, pp. 97–128.

[15] I. Kymissis. *Organic Field Effect Transistors : Theory, Fabrication and Characterization*. Integrated Circuits and Systems. 2009.

[16] G.J. Conibeer and A. Willoughby, eds. *Solar cell materials: developing technologies*. Wiley series in materials for electronic and optoelectronic applications. 2014.

[17] A. Goetzberger, B. Voß, and J. Knobloch. *Sonnenenergie: Photovoltaik: Physik und Technologie der Solarzelle*. Teubner, 1997.

[18] `http://plasticphotovoltaics.org`. Accessed: 14.05.2018.

[19] A.C. Mayer, S.R. Scully, B.E. Hardin, M.W. Rowell, and M.D. Mcgehee. "Polymer-based solar cells". In: *Materials Today* 10.11 (2007), pp. 28–33.

[20] W. Shockley and H.J. Queisser. "Detailed Balance Limit of Efficiency of p-n Junction Solar Cells". In: *Journal of Applied Physics* 32.3 (1961), pp. 510–519.

[21] A. Polman, M. Knight, E.C. Garnett, B. Ehrler, and W.C. Sinke. "Photovoltaic materials: Present efficiencies and future challenges". In: *Science* 352.6283 (2016).

[22] R. Farchioni and G. Grosso, eds. *Organic electronic materials : conjugated polymers and low molecular weight organic solids*. Vol. 41. Springer series in materials science. Berlin: Springer, 2001.

[23] D.A. Stone, Y. Chang, and H.R. Allcock. "Control of the conjugation length and solubility in electroluminescent polymers". In: *Journal of Polymer Science Part A: Polymer Chemistry* 44.1 (2005), pp. 69–76.

[24] M.A. Green, E.D. Hishikawa Y.and Dunlop, D.H. Levi, J. Hohl-Ebinger, and A.W.Y. Ho-Baillie. "Solar cell efficiency tables (version 52)". In: *Progress in Photovoltaics: Research and Applications* 26.7 (2018), pp. 427–436.

[25] C.W. Tang, S.A. VanSlyke, and C.H. Chen. "Electroluminescence of doped organic thin films". In: *Journal of Applied Physics* 65.9 (1989), pp. 3610–3616.

[26] J.J.M. Halls, K. Pichler, R.H. Friend, S.C. Moratti, and A.B. Holmes. "Exciton diffusion and dissociation in a poly(p-phenylenevinylene)/C60 heterojunction photovoltaic cell". In: *Applied Physics Letters* 68.22 (1996), pp. 3120–3122.

[27] A. Haugeneder, M. Neges, C. Kallinger, W. Spirkl, U. Lemmer, J. Feldmann, U. Scherf, E. Harth, A. Gügel, and K. Müllen. "Exciton diffusion and dissociation in conjugated polymer/fullerene blends and heterostructures". In: *Physical Review B* 59.23 (1999), pp. 15346–15351.

[28] S. Hüfner. *Photoelectron spectroscopy : principles and applications*. 3rd rev. and enl. ed. Advanced texts in physics. Berlin: Springer, 2003.

[29] S. Suga. *Photoelectron Spectroscopy : Bulk and Surface Electronic Structures*. Vol. 176. Springer Series in Optical Sciences. 2014.

[30] P. Strobel. *Fullerene als alternative Akzeptoren bei der Transferdotierung von Diamantoberflächen*. 2008.

[31] P.D. Johnson and J.W. Davenport. "Calculated inverse photoemission cross sections from adsorbed molecules". In: *Physical Review B* 31.12 (1985), pp. 7521–7525.

[32] P. Hofmann. *Surface Physics: An Introduction*. 2013.

[33] A. Zangwill. "Clean surfaces". In: *Physics at Surfaces*. Cambridge: Cambridge University Press, 1988, pp. 5–6.

[34] A. Jablonski and C.J. Powell. "Information depth and the mean escape depth in Auger electron spectroscopy and x-ray photoelectron spectroscopy". In: *Journal of Vacuum Science & Technology A: Vacuum, Surfaces, and Films* 21.1 (2003), pp. 274–283.

[35] J. Als-Nielsen. *Elements of modern X-ray physics*. 2nd ed. Chichester: Wiley, 2011.

[36] P. Willmott. *An introduction to synchrotron radiation : techniques and applications*. Chichester, 2011.

[37] S. Mobilio. *Synchrotron Radiation : Basics, Methods and Applications*. 2015.

[38] R.E. Dinnebier and S.J.L. Billinge, eds. *Powder diffraction: theory and practice*. Cambridge: Royal Society of Chemistry, 2008.

[39] A. Madsen. "Europe enters the extreme X-ray era". In: *CERN Courier* 57.6 (2017), pp. 19–23.

[40] M. Altarelli et al., ed. *XFEL: the European X-ray free-electron laser - technical design report*. `http://xfel.desy.de/technical_information/tdr/tdr/.`. 2006.

[41] M.J. Druyvesteyn. "Das Röntgenspektrum zweiter Art". In: *Zeitschrift für Physik* 43.9 (1927), pp. 707–725.

[42] F. Bloch and P.A. Ross. "Radiative Auger Effect". In: *Phys. Rev.* 47 (11 1935), pp. 884–885.

[43] Australian Synchrotron. `http://www.synchrotron.org.au`.

[44] J. Eccher, W. Zajaczkowski, G.C. Faria, H. Bock, H. von Seggern, W. Pisula, and I.H. Bechtold. "Thermal Evaporation versus Spin-Coating: Electrical Performance in Columnar Liquid Crystal OLEDs". In: *ACS Applied Materials & Interfaces* 7.30 (2015), pp. 16374–16381.

[45] B. Nabet. *Photodetectors : materials, devices and applications*. 2016.

[46] `https://aavos.eu/glossary/uv-vis-spectrometry/`. Accessed: 26.06.2018.

[47] D. Hoffman. *Handbook of vacuum science and technology*. San Diego, CA, 1998.

[48] N. Yoshimura. *Vacuum Technology: Practice for Scientific Instruments*. Berlin, Heidelberg: Springer Berlin Heidelberg, 2008.

[49] P.D. Johnson and S.L. Hulbert. "Inverse photoemission". In: *Review of Scientific Instruments* 61.9 (1998), pp. 2277–2288.

[50] G. Dongping, Y. Yingguo, L. Shuhu, H. Caihao, and G. Xingyu. "An Efficient monochromatic Electron Source designed for Inverse Photoemission Spectroscopy". In: *Chinese Physics C* 38.11 (2014).

[51] M. Schmid, H.-P. Steinrück, and J.M. Gottfried. "A new asymmetric Pseudo-Voigt function for more efficient fitting of XPS lines". In: *Surface and Interface Analysis* 46.8 (2014), pp. 505–511.

[52] R. Hesse, P. Streubel, and R. Szargan. "Product or sum: comparative tests of Voigt, and product or sum of Gaussian and Lorentzian functions in the fitting of synthetic Voigt-based X-ray photoelectron spectra". In: *Surface and Interface Analysis* 39.5 (2007), pp. 381–391.

[53] J. Végh. "The Shirley background revised". In: *Journal of Electron Spectroscopy and Related Phenomena* 151.3 (2006), pp. 159–164.

[54] J. Walton, M.R. Alexander, N. Fairley, P. Roach, and A.G. Shard. "Film thickness measurement and contamination layer correction for quantitative XPS". In: *Surface and Interface Analysis* 48.3 (2016), pp. 164–172.

[55] SPECS. *Thickness determination of multi-layered systems*. http://www.specs.de/cms/upload/PDFs/ApplNotes/PHOIBOS/TNote-OverlayerThickness.pdf. Accessed: 15.06.2018.

[56] S. Tanuma, C.J. Powell, and D.R. Penn. "Calculations of electron inelastic mean free paths. V. Data for 14 organic compounds over the 50-2000 eV range". In: *Surface and Interface Analysis* 21.3 (1994), pp. 165–176.

[57] V. Santana. [UV-Vis measurements of curcumin and bixin on solution-cast films and in solution]. Unpublished raw data. 2018.

[58] NREL. http://rredc.nrel.gov/solar/spectra/am1.5/. Accessed: 13.06.2018.

[59] R. Waranyoupalin, S. Wongnawa, M. Wongnawa, C. Pakawatchai, P. Panichayupakaranant, and P. Sherdshoopongse. "Studies on complex formation between curcumin and Hg(II) ion by spectrophotometric method: A new approach to overcome peak overlap". In: *Open Chemistry* 7.3 (2009), p. 2433.

[60] P. Thu Ha, T.M. Nguyet Tran, H.D. Pham, Q.H. Nguyen, and X.P. Nguyen. "The synthesis of poly(lactide)-vitamin E TPGS (PLA-TPGS) copolymer and its utilization to formulate a curcumin nanocarrier". In: *Advances in Natural Sciences: Nanoscience and Nanotechnology* 1.1 (2010).

[61] W. Rahmalia, J.-F. Fabre, and Z. Mouloungui. "Effects of Cyclohexane/Acetone Ratio on Bixin Extraction Yield by Accelerated Solvent Extraction Method". In: *Procedia Chemistry* 14 (2015), pp. 455–464.

[62] W. Rahmalia, J.-F. Fabre, T. Usman, and Z. Mouloungui. "Adsorption Characteristics of Bixin on Acid- and Alkali-Treated Kaolinite in Aprotic Solvents". In: *Bioinorganic Chemistry and Applications* 3 (2018), pp. 1–9.

[63] G Scheibe. "Über die Veränderlichkeit der Absorptionsspektren in Lösungen und die Nebenvalenzen als ihre Ursache". In: *Angewandte Chemie* 50.11 (Mar. 1937), pp. 212–219.

[64] F. Würthner, T.E. Kaiser, and C.R. Saha-Möller. "J-Aggregates: From Serendipitous Discovery to Supramolecular Engineering of Functional Dye Materials". In: *Angewandte Chemie International Edition* 50.15 (2011), pp. 3376–3410.

[65] W. Rahmalia, J.-F. Fabre, T. Usman, and Z. Mouloungui. "Aprotic solvents effect on the UV–visible absorption spectra of bixin". In: *Spectrochimica Acta Part A: Molecular and Biomolecular Spectroscopy* 131 (2014), pp. 455–460.

[66] J.F. Moulder, W.F. Stickle, P.E. Sobol, and K.D. Bomben. *Handbook of X-ray Photoelectron Spectroscopy – A Reference Book of Standard Spectra for Identification and Interpretation of XPS Data*. Eden Prairie, Minnesota: Perkin-Elmer Corporation, 1995, pp. v–v.

[67] https://vuo.elettra.eu/services/elements/WebElements.html. Accessed: 17.07.2018.

[68] P.G. Rouxhet and M.J. Genet. "XPS analysis of bio-organic systems". In: *Surface and Interface Analysis* 43.12 (2011), pp. 1453–1470.

[69] H. Hoppe and N.S. Sariciftci. "Organic solar cells: An overview". In: *Journal of Materials Research* 19.07 (2004), pp. 1924–1945.

[70] D. Wöhrle and D. Meissner. "Organic Solar Cells". In: *Advanced Materials* 3.3 (1991), pp. 129–138.

[71] G.S. Pawley. “Unit-cell refinement from powder diffraction scans”. In: *Journal of Applied Crystallography* 14.6 (1981), pp. 357–361.

[72] J.W. Reid, J.A. Kaduk, S.V. Garimella, and J.S. Tse. “Rietveld refinement using synchrotron powder diffraction data for curcumin, C21H20O6, and comparison with density functional theory”. In: *Powder Diffraction* 30.01 (2014), pp. 67–75.

[73] N. Widjonarko. “Introduction to Advanced X-ray Diffraction Techniques for Polymeric Thin Films”. In: *Coatings* 6.4 (2016).

[74] A. Häberli and H. Pfander. “Synthesis of Bixin and Three Minor Carotenoids from Annatto (Bixa orellana)”. In: *Helvetica Chimica Acta* 82.5 (1999), pp. 696–706.